

UC Riverside

UC Riverside Electronic Theses and Dissertations

Title

Virus-Resembling Nano-Structures for Fluorescence Imaging of Ovarian Cancer

Permalink

<https://escholarship.org/uc/item/2x94j2vk>

Author

Guerrero, Yadir Alejandro

Publication Date

2015

Peer reviewed|Thesis/dissertation

UNIVERSITY OF CALIFORNIA
RIVERSIDE

Virus-Resembling Nano-Structures for Fluorescence Imaging of Ovarian Cancer

A Dissertation submitted in partial satisfaction
of the requirements for the degree of

Doctor of Philosophy

in

Bioengineering

by

Yadir Alejandro Guerrero

March 2016

Dissertation Committee:

Dr. Bahman Anvari, Chairperson

Dr. Ameae M. Walker

Dr. Valentine I. Vullev

Copyright by
Yadir Alejandro Guerrero
2016

The Dissertation of Yadir Alejandro Guerrero is approved:

Committee Chairperson

University of California, Riverside

ACKNOWLEDGEMENTS

This study would not have been possible without the continuous support, patience and guidance of many people. I would like to begin by acknowledging the efforts of all faculty and staff in the bioengineering department whose efforts ensure the availability to funds and learning opportunities. I would like to thank my dissertation committee, Dr. Bahman Anvari, Valentine Vullev, and Ameae Walker for your continued support and guidance. It is in large part to Dr. Anvari's high standards that I have been able to grow and I express my deepest gratitude for his patience and commitment to my academic development.

I am grateful to the Anvari Biophotonics Lab for their continued support and aid during critical times. I would like to make special note of Dr. Baharak Bahmani with whom I worked closely bouncing ideas back and forth allowing for both of us to grow and learn the past five years. Special thanks to all of the undergraduate students who have contributed to this work; Leela Tanikella, Sara Said, Truong Mai, and Edver Bahena. Teaching and providing guidance to each of them has been the most rewarding experience of my career and they have proven pivotal in the completion of this work. I am thankful for the guidance and support I have received from several professors including Dr. Victor Rodgers and Dr. Hyle Park. I would also like to thank Mrs. Hong Xu, whose light-hearted nature has made some difficult situations much easier to manage. Lastly, I would like to thank my wife Ana Laura Guerrero for whom no words can express my gratitude.

ABSTRACT OF THE DISSERTATION

Virus-Resembling Nano-Structures for Fluorescence Imaging of Ovarian Cancer

by

Yadir Alejandro Guerrero

Doctor of Philosophy, Graduate Program in Bioengineering
University of California, Riverside, March 2016
Dr. Bahman Anvari, Chairperson

The use of nanosized materials for the diagnosis and treatment of disease has grown exponentially in recent years. Biologically derived materials, more specifically, plant virus constructs offer several advantages as tools for nanomedicine including the ability to self-assemble into highly monodisperse structures with discrete shape and size containing highly addressable surfaces for chemical or biological modification. NIR dye encapsulating nanoconstructs have demonstrated their importance as effective agents for deep tissue optical imaging in the early detection of cancers allowing for the visualization of small (>5mm) tumors. Encapsulation mitigates the deficiencies of organic NIR dyes by shielding them, increasing chemical and photostability, while decreasing clearance rates, and making hydrophilicity issues irrelevant. The objective of this study is to investigate the effectiveness of an optical nano-structured system for targeted near infrared (NIR) imaging of ovarian cancer cells that over-express the human epidermal growth factor receptor 2 (HER2), an important biomarker associated with ovarian cancer. The nano-structured system, optical viral ghosts (OVGs), is comprised of the genome-

depleted plant-infecting brome mosaic virus (BMV) doped with NIR chromophore, indocyanine green (ICG), and functionalized at the surface by covalent attachment of monoclonal antibodies against the HER2 receptor. We use absorption, fluorescence spectroscopy, and dynamic light scattering to characterize the physical properties of the constructs. Using fluorescence imaging and flow cytometry, we demonstrate the effectiveness of these nano-structures for targeted NIR imaging of HER2 receptors *in vitro*. After demonstrating the effectiveness of these ICG doped nano-constructs *in-vitro* we investigate their payload flexibility and their potential for *in-vivo* use. Optimized fabrication parameters for the loading of two organic NIR dyes (ICG and BrCy-106) were established based on ϕ -value (ratio of capsid protein concentration: dye concentration) to produce nano-structures with the highest fluorescence emission. Despite the lack of specific targeting moieties OVGs localized to ovarian cancer nodules in nu/nu mice *in-vivo* more successfully than the corresponding unloaded dye. Ovarian cancer remains the dominant cause of death due to malignancies of the female reproductive system. The capability to identify and remove all tumors during intraoperative procedures may ultimately reduce cancer recurrence, and lead to increased patient survival. Our virus-resembling nano-structures could potentially be used for early detection and fluorescence guided cytoreduction surgery.

TABLE OF CONTENTS

CHAPTER 1: INTRODUCTION	1
CHAPTER 2: Virus-Resembling Nano-Structures for Near Infrared Fluorescence Imaging of Ovarian Cancer HER2 Receptors	6
2.1 INTRODUCTION	6
2.2 EXPERIMENTAL SECTION	9
2.2.1 Reagents.....	9
2.2.2 Fabrication of OVGs.....	9
2.2.2.1 Virus purification	10
2.2.2.2 Virus disassembly	11
2.2.2.3 Separating viral RNA from CP.....	11
2.2.2.4 Capsid reassembly and ICG encapsulation.....	12
2.2.3 Functionalization of OVGs	13
2.2.4 Characterization of OVGs.....	15
2.2.5 Cell Lines and Fluorescence Microscopy	16
2.2.6 Flow Cytometry	18
2.3 RESULTS AND DISCUSSION	18
2.3.1 Characterization of OVGs.....	18
2.3.2 OVG Functionalization and Specificity for HER2	23
2.3.3 Quantification of HER2 Targeting.....	26
2.4 CONCLUSIONS.....	31
2.5 SUPPLEMENTAL INFORMATION	31
2.5.1 Virus propagation.....	31
2.5.2 Selection of ICG concentration for encapsulation into optical viral ghosts (OVGs), and photo-excitation wavelength	32
2.5.3 Estimating the number of OVGs.....	34
2.5.4 Estimating the number of ICG per OVG	36
2.5.5 Immunohistochemical staining of OVGs.....	36
2.5.6 Flow cytometry results.....	38

CHAPTER 3: Virus-Mimicking Nano-Constructs as Platforms for NIR

Fluorescence Imaging of Stage I- Sized Ovarian Cancer Tumors	40
3.1 INTRODUCTION	40
3.2 METHODS	42
3.2.1 Reagents	43
3.2.2 OVG Fabrication.....	43
3.2.3 Spectroscopy	44
3.2.4 Animal Protocol.....	44
3.2.5 Organ Analysis.....	45
3.3 Results and Discussion	46
3.3.1 Dye Characterization	46
3.3.2 BrCy-106 OVG Encapsulation	51
3.3.3 Optimizing Dye Encapsulation	53
3.3.4 In-vivo Nano-construct Delivery	56
3.4 CONCLUSIONS.....	60
CHAPTER 4: CONCLUSION.....	62
REFERENCES.....	64

LIST OF FIGURES

Figure 1 Schematic of specific cell-surface receptor targeting by functionalized OVGs... 8

Figure 2 BMV dissociation, purification and self-assembly of OVGs. OVG fabrication from purified BMV. (1) Dialyze the BMV virions against disassembly buffer (24 hours); (2) centrifuge at low-speed ($\approx 18,200 \times g$ (relative centrifugal force (RCF)) (30 minutes) to remove un-dissociated BMV and large RNA chunks; (3) remove un-dissociated BMV particles by high-speed centrifugation ($\approx 262,000 \times g$ RCF, one hour) and collect supernatant containing dissociated capsid proteins (CP); (4) dialyze against pH=7.2 RNA re-assembly buffer to remove residual RNA; (5) discard pellet containing reassembled BMV by high-speed centrifugation ($\approx 262,000 \times g$ RCF, one hour); (6) collect supernatant containing purified dissociated BMV CP; (7) add ICG to the solution at specified \square -ratio (concentration of CP to that of ICG); (8) dialyze against BMV assembly buffer (24 hours) to assemble virus-like-particles; (9) remove excess ICG and dissociated CP by high-speed centrifugation ($\approx 262,000 \times g$ RCF, one hour), and keep the pellet containing intact OVGs; (10) re-suspend OVGs in BMV suspension buffer solution. 10

Figure 3 Surface functionalization of OVGs with anti-HER2 monoclonal antibody. (1) Equal number of single-aldehyde terminated (5 kDa), and double-aldehyde terminated (10 kDa) PEG polymers are added to OVGs in BMV suspension buffer followed by anti-HER2 monoclonal antibodies and 14 μ l of 20 mM sodium dithionite. The reaction is allowed to age for one hour at 4°C in dark. (2) Sample is subsequently dialyzed in OVG Suspension buffer for six hours using a 300 kDa MW-cutoff dialysis membrane. (3) After dialysis, sample is centrifuged to remove any unbound components, and recover functionalized OVGs..... 14

Figure 4 (a) Absorption, and (b) normalized fluorescence emission spectra of non-functionalized OVGs, anti-HER2-functionalized OVGs, anti-HER2 monoclonal antibody (300 ng/ml), and 13 μ M ICG in response to photo-excitation at 680 nm. Solvent was OVG suspension buffer in all cases. The ϕ -value used to fabricate both non-functionalized and functionalized OVGs was 200. 19

Figure 5 Diameter distributions of non-functionalized OVG, anti-HER2-functionalized OVGs, and wild type BMV as determined by dynamic light scattering. We present the mean of three measurements on three identically prepared samples with error bars representing the standard deviations from the mean. We fitted Lorentzian functions to the measured diameter distributions (solid curves). The ϕ -value used to fabricate both non-functionalized and functionalized OVGs was 200..... 22

- Figure 6 Fluorescence image of SKOV-3 cell line after two hours of incubation with anti-HER2-functionalized OVGs. Individual panels show: (a) DAPI-stained cell nuclei (blue), (b) FITC-labeled secondary antibody (green), (c) anti-HER2-functionalized OVGs (red), and (d) merged images. Scale bars correspond to 20 μm . The ϕ -value used to fabricate both non-functionalized and functionalized OVGs was 10. 24
- Figure 7 Fluorescent images of (a) SKOV-3 cells following one hour of incubation at 37 $^{\circ}\text{C}$ with (i) free ICG, (ii) non-functionalized OVGs, and (ii) anti-HER2-functionalized OVGs. (b) Merged bright-field and NIR fluorescence images of (i) OVCAR-3, and (ii) SKOV-3 cell lines incubated with functionalized OVGs for 45 minutes at 4 $^{\circ}\text{C}$.. (c) NIR fluorescence images of co-cultures of OVCAR-3 and SKOV-3 cell populations after 30 minutes of incubation at 37 $^{\circ}\text{C}$ with (i) OVGs, and (ii) functionalized OVGs. The boxed region in panel (c(ii)) points to a dead OVCAR-3 cell. For both (a) and (b) the ϕ -value used to fabricate both non-functionalized and functionalized OVGs was 10 and 200 in (c). Blue false-colour indicates the presence of DAPI while the red false-colour indicates NIR emission. All scale bars correspond to 20 μm 25
- Figure 8 Quantification of HER2 targeting by flow cytometry. (a) The relative mean fraction of the populations (N) of SKOV-3 and OVCAR-3 cells emitting NIR fluorescence signal after 45 minutes of incubation at 4 $^{\circ}\text{C}$ with suspension buffer (negative control), ICG (positive control), OVGs, and functionalized OVGs. (b) The relative mean fraction of the populations (N) of SKOV-3 cells emitting NIR fluorescence after incubation for two hours at 37 C with ICG, OVGs, and anti-HER2-functionalized OVGs. Incubation with functionalized OVGs was performed in the absence, or presence of 300 ng or 1.2 μg of anti-HER2 antibody. Error bars represent the standard deviations from the mean for triplicate samples. Asterisks represent statistically significant differences between the indicated pairs (p-value < 0.05). The ϕ value used to fabricate both non-functionalized and functionalized OVGs was 10. 28
- Figure 9 Barley is seeded at day one in sterile nutrient rich soil, and placed in a controlled green house. At day seven, the seedling is between 2-3 inches in height at which point the single leaf is mechanically disturbed with the use of carborundum, and the virus is introduced directly into the cell. By day 15, signs of infection begin to appear in the form of a brome mosaic pattern. By week three, depending on the degree of infection, the plants are ready for collection..... 32
- Figure 10 (a) Concentration-dependent fluorescence emission intensities of ICG at 700 and 790 nm, corresponding to H-Like and monomeric forms of ICG, respectively. Solvent was OVG suspension buffer. We fitted the measured spectra with Lorentzian distribution functions. (b) Excitation-emission map for 8 μM free ICG dissolved in OVG suspension buffer. 33

Figure 11 Immunohistochemical staining of functionalized-OVG with goat-anti-rabbit alkaline phosphatase conjugated secondary antibody. Color change indicated alkaline phosphatase activity. Samples include (a) suspension buffer, (b) non-functionalized OVGs, (c) free alkaline-phosphatase conjugated antibody and (d) anti-HER2-functionalized OVGs. The ϕ value used to fabricate both non-functionalized and functionalized OVGs was 10. Both types of OVGs were fabricated using a single fabrication method.	38
Figure 12 The number of OVCAR3 and SKOV3 cell exhibiting ICG fluorescent signals as determined by flow cytometry. We present the results for OVCAR3 (a) and SKOV3 (b) cells after 45 minutes of incubation at 4 °C with OVG suspension buffer (negative control), ICG (positive control), OVGs, and anti-HER2-functionalized OVGs. In panel (c), SKOV3 cells were incubated with ICG, OVGs, functionalized OVGs, and anti-HER2f-functionalized OVGs for 2 hours at 37 °C. Incubation with the functionalized OVGs was performed in the absence, or presence of 300 ng or 1.2 μ g of anti-HER2 antibody.	39
Figure 13 Excitation emission map for (a) BrCY-106 and (b) ICG in water. Both dyes were excited from 600-800nm but excitation was collected from 720-850nm and 650-900nm for BrCY-106 and ICG respectively.....	47
Figure 14 (a) Linear fit for peak absorbance of BrCy-106 (745nm) with water and OVG Suspension buffer as diluents. (b) Comparison of peak absorbance for BrCY-106 and ICG in OVG Suspension Buffer at 745nm and 780nm respectively. Absorbance spectra for variable dilutions of (c) BrCy-106 and (d) ICG in OVG Suspension Buffer.....	49
Figure 15 (a) Comparison of BrCy-106 and ICG peak emission at 775nm and 780nm after excitation at 680nm and 730nm respectively. Inset of (a) shows considerably lower ICG peak emission. (b) Integrated emission in the range of 735nm to 900nm for BrCy-106 and ICG.	50
Figure 16 Integrated emission of short and long term storage of BrCy-106. Dye storage for (a) six hours at 4°C and (b) one year at -20°C.	51
Figure 17 Comparison of encapsulation efficiency of ICG and BrCy-106 within OVGs. (a) Absorbance and (b) emission spectra of ICG encapsulating OVGs [OVGs (ICG)], BrCY-106 encapsulating OVGs [OVGs (BrCy-106)] and their corresponding supernatants after washing in response to 680nm excitation. (c) Integrated emission from 700-900nm of OVGs doped with BrCy-106 and ICG and their respective supernatants. (d) Hydrodynamic diameters of ICG and BrCY-106 doped OVGs, with n=3 measurements. OVGs were formulated at ϕ =200 with 10 μ g/ml of dye and 2mg/ml of capsid protein.....	52

Figure 18 OVG ϕ -formulations in the 4-1000 range with dye held constant at 5 μ g/ml and varying capsid protein concentrations. (a) Integrated emission of OVGs encapsulating BrCy-106 and ICG and the respective integrated emission ratio for each surveyed ϕ -value. Characteristic peak absorbances for (b) ICG at 800nm and (c) BrCy-106 at 745nm including peak values for capsid protein at 280nm. 55

Figure 19 OVG ϕ -formulations in the 10-1000 range with capsid protein held constant at 1mg/ml and varying dye concentrations. (a) Integrated emission of OVGs encapsulating BrCy-106 and ICG and the respective integrated emission ratio for each surveyed ϕ -value. Cha Characteristic peak absorbances for (b) ICG at 800nm and (c) BrCy-106 at 745nm including peak values for capsid protein at 280nm. 56

Figure 20 (a) Absorbance spectra of samples used for mice studies. All measurements are shown at a 1:10 dilution. Average emission spectra of n=5 homogenized tumors after 720nm excitation presented as (b) a spectra and (c) histogram form after weight normalization. (d) Image analysis using fitted ROIs of tumor samples on n=2 data set. Two-tailed t-test was performed on the data with p< 0.05 indicated by (*). 58

Figure 21 Histogram of dye distribution in mice. Data corresponds to image processing using fitted ROIs on n=5 data set. 60

CHAPTER 1: INTRODUCTION

Expected to surpass heart disease as the leading cause of death in the United States within the next few years with 1,658,370 estimated new cases and 589,430 deaths per year, cancer is a constantly growing health concern.¹ Regardless of localization area, early cancer detection is indispensable for successful treatment and reduced disease recurrence rates. For certain cancers current clinical detection which relies on computed tomography, magnetic resonance imaging, x-ray, ultrasound or positron emission tomography for diagnosis may prove adequate despite its lack of sensitivity and at times limited toxicity. Increased sensitivity and specificity may prove crucial in diseases such as ovarian cancer where only 20% of cases are diagnosed before metastasis at stage I and have limited survival (20%) when diagnosed at higher stages (II-IV).^{2, 3} Several new optical imaging methods are being developed as potential alternatives for early detection of disease.⁴ Optical imaging methods that rely on NIR light (~650-1450nm) are especially advantageous due to low absorbance and autofluorescence of biological tissues within this range resulting in increased light penetration, sensitivity and decreased signal to noise ratio as a result of decreased background interference.^{5, 6}

An NIR dye of particular importance due to its broad range of applications and sustained use since the late 1950's⁷, Indocyanine Green (ICG) ($C_{43}H_{47}N_2NaO_6S_2$; molecular weight ~ 775 Da) remains the only NIR dye approved by the FDA for cardiovascular measurements, liver function tests and ophthalmological imaging.^{8, 9} ICG is currently being investigated for use outside of its established clinical applications for early cancer detection and aide in surgical procedures¹⁰. It is therefore not unreasonable

to set ICG as a reference point when evaluating the potential of new organic NIR dyes as tools for translational work that span the spectrum from bench side, to small animal, to clinical applications. For cancer biology applications organic NIR dyes should ideally have high molar absorption coefficients and quantum yield, be chemically stable and photostable under biological conditions and possess good hydrophilicity to reduce dye aggregation.^{11, 12} Despite its ubiquitous use ICG has a relatively low quantum yield (~0.3-4.3%)¹³ among other commercially available NIR dyes such as IR800dye (~10%)¹⁴ and especially low when compared dyes emitting at shorter wavelengths such as Cy7 (28%), Cy5 (18%), Alexa Fluor 700 (25%).⁵ Apart from its lower emission intensities ICG suffers from several other drawbacks including aqueous instability, chemical and photo-degradation, self-aggregation and high protein binding all leading to increased clearance from plasma (half-life ~ 2-4 minutes),¹⁵⁻¹⁹ thus limiting its clinical efficacy. Shielding of ICG has been investigated as a possible method to increase its use under biological conditions with encapsulation proving a valid strategy. Our group has previously reported the encapsulation of ICG in synthetic polymer-based nano-constructs²⁰⁻²², red-blood cell derived vesicles,²³ as well as virus-resembling nano-structures.²⁴⁻²⁶

The second chapter of this thesis investigates the use of virus-resembling nanostructures as potential optical probes for the specific targeting of ovarian cancer derived cell-lines featuring over-expression of HER2 receptors. We use absorption, fluorescence spectroscopy, and dynamic light scattering to characterize the physical properties of the constructs. Using fluorescence imaging and flow cytometry, we demonstrate the effectiveness of these nano-structures for targeted NIR imaging of HER2 receptors in

vitro. We were able to present the first results that demonstrate successful functionalization of OVGs with anti-HER2. Our results indicate an increase in size of OVGs from $24 \text{ nm} \pm 3$ to $37.5 \pm 3.6 \text{ nm}$ upon functionalization of the OVG surface. We demonstrate the specificity and sensitivity of our constructs through a competitive study in which we incubate SKOV-3 (high-HER2 expression) cells at 37°C for 2 hours with a constant amount of functionalized OVGs and an increasing amount of competitive antibody. When an amount of antibody equal to that used for fabrication was added uptake of functionalized OVGs resembled the uptake of bare OVGs by SKOV-3 cells. When an excess amount of competitive antibody was used the uptake of functionalized OVGs more closely resemble the uptake of free ICG. While we focused on functionalization of OVGs with anti-HER2 in this study the chemistry used does not limit us to any one antibody or protein targeting moiety, meaning OVGs can potentially be functionalized with an array of targeting moieties with potential for imaging various cancer types.

In chapter three, we look towards the application of OVGs for *in-vivo* tumor detection. Unpublished preliminary work done in nu/nu nude mice hinted at the difficulties associated with detection of small tumors ($>5\text{mm}$) *in-vivo* using our nano-constructs when loaded with ICG. Most of the work presented in chapter 2 was based on OVGs with a ϕ -value of 10 (concentration of capsid protein/ concentration of dye) with initial dye concentrations of $10\mu\text{g/ml}$ and a corresponding capsid protein concentration of $100\mu\text{g/ml}$. Concerns with ϕ -value of 10 OVGs arose, including a low fluorescence emission and a low total number of particles. Since OVGs are highly uniform self-

assembling vehicles there is a directly proportional increase in the total number of particles fabricated with increasing capsid protein, therefore using such low concentrations of protein would result in a low number of nanoparticles. In chapter three we address these concerns and carry out a detailed study to determine the concentrations of dye and capsid protein to achieve fabrication of OVGs with maximum fluorescence emission. We determined the optimal ϕ -value to be between 200 and 500 with initial ICG concentration between 5-7 μ g/ml. Despite the advantages of encapsulating ICG its drawbacks remain present to a lessened degree. Among the still present concerns are the overall relative emission levels and issues of dye aggregation which are amplified in a reduced nano-environment. In order to more efficiently image small cancer nodules in a small animal model we make use of BrCy-106 (C₃₆H₄₂Br₂N₂O₃S₃; molecular weight ~935 Da), a new organic NIR dye from Nanoquantum Sciences. Its spectral properties include absorption and emission maximum at 745 and 775nm respectively in phosphate buffer and a quantum yield 4-5 times higher than ICG (16%). Furthermore, BrCy-106 does not suffer from chemical stability issues in aqueous buffer and most importantly its tendency to self-aggregate is considerably lower. We explored the use of a recently developed dye, BrCy-106, both in its free form and when doped into OVGs. The virus-resembling nano-structures doped with BrCy-106 remained monodisperse, exhibited sub-30nm diameter and remained biocompatible with the added benefit of superior (10-20 fold) increase in NIR fluorescence emission as compared to ICG doped OVGs. We found that despite the lack of specific targeting moieties our nano-structures localized to ovarian cancer nodules in nu/nu mice *in-vivo* more successfully than the corresponding unloaded

dye. BrCy-106 delivered in either form allowed for clearer visualization of tumor nodules when compared to ICG demonstrating the potential to serve as a new optical contrast agent for early cancer detection.

In summary, the studies shown here show the first use of Brome Mosaic Virus derived virus-resembling nano-structures as near-infrared optical probes for the specific targeting of ovarian cancer biomarker receptors. Constructs derived from replication deficient plant viruses are especially attractive since plant viruses do not infect humans ²⁷, and constructs containing plant virus components are expected to be biocompatible and biodegradable in mammalian systems ²⁸⁻³⁰. To the best of our knowledge this is the first use of BMV virus-resembling nanoconstructs used for the detection of small (>5mm) cancer nodules in a small animal model. These constructs could help improve early detection and disease management by providing the capability for detection and imaging of otherwise undetectable nodules.

CHAPTER 2: Virus-Resembling Nano-Structures for Near Infrared Fluorescence Imaging of Ovarian Cancer HER2 Receptors

2.1 INTRODUCTION

Ovarian cancer causes more deaths than any other malignancy affecting the female reproductive system³¹. Only about 20% of ovarian cancers are diagnosed at stage I when the disease is still confined to the ovaries³². For cancers classified at higher stages (II-IV), when the disease has spread beyond the ovaries, the overall five-year survival rate is less than 20%³². Treatment of ovarian cancer is based on cytoreductive surgery to remove all of the tumors, followed commonly by chemotherapy^{33, 34}. The degree of success in cytoreductive surgery is an important prognostic factor, with improved survival associated with complete resection of all visible cancer^{35, 36}. Current surgical standard is removal of all visible deposits, which are on the order of 1-2 cm nodules. Detection of small intraperitoneal tumor deposits (diameter <1 mm) remains a great challenge during cytoreductive surgery. These small nodules are difficult to detect pre-operatively by current imaging methods based on ultrasound, computed tomography (CT), magnetic resonance (MR), or visually at surgery. If not removed during surgery, tumor recurrence can occur, which is unfortunately common with this disease.

Imaging methods that can identify small diameter tumors offer the potential for enhanced diagnosis and ultimately improved therapeutic outcome. One such method is fluorescence imaging using optical contrast agents with emission in the near infrared (NIR) spectral range (~700-1450 nm). These materials offer two key advantages: (1)

given that there is reduced NIR auto-fluorescence ⁶, use of exogenous materials that are photo-excited in NIR spectral band will lead to enhanced imaging contrast; and (2) due to reduced absorption by water and proteins as well as diminished scattering in the spectral window between about 700-1450 nm ⁶, use of NIR wavelengths enable increased optical penetration allowing visualization of tumor nodules up to 2-3 cm below the surface ^{37, 38}.

One particular material for NIR imaging is indocyanine green (ICG). To date, ICG remains as the only NIR FDA-approved dye for specific imaging applications ^{8, 10}. By combining ICG with an ovarian cancer specific targeting moiety, it may be possible to develop a platform for molecular imaging of a biomarker to identify small tumor nodules. A potential ovarian cancer biomarker is human epidermal growth factor receptor-2 (HER2). Using flow cytometry, western blot analysis, and quantitative-polymerase chain reaction (q-PCR) methods, a recent study reports the expression of HER2 in all tumor cells derived from solid tumors and primary ascites, as well as all established and short-term cultured cancer cells ³⁹. Increased HER2 expression has been correlated with reduced survival time ⁴⁰⁻⁴², and increased risk of progression and death ⁴².

We have engineered a nano-scale platform that integrates NIR imaging and molecular recognition capabilities. Specifically, the platform consists of ICG encapsulated by capsid proteins (CPs) derived from genome-depleted plant-infecting brome mosaic virus (BMV) ^{24, 25}. We refer to these constructs as optical viral ghosts (OVGs) since only the CP subunits of the virus are used to encapsulate the ICG molecules. Methodologies for disassembly of bromoviridae family of viruses, which include the BMV, and the re-assembly of purified CP subunits into nanoscale structures

⁴³, and fabrication of plant virus-like particles loaded with imaging or therapeutic agents have been under extensive investigations ⁴⁴⁻⁴⁸. Viral protein based materials, specifically those derived from plant viruses, provide a highly versatile platform that can be chemically and biologically modified to obtain numerous functionalities without innate immunogenicity concerns associated with mammalian viruses ³⁰. Herein, we demonstrate the effectiveness of OVGs functionalized with monoclonal antibodies against HER2 receptor as nano-probes for targeted molecular imaging of HER2-expressing ovarian cancer cells in-vitro. A conceptual scheme of the putative specific molecular targeting capability of functionalized OVGs to HER2 cell membrane receptors is presented in Figure 1.

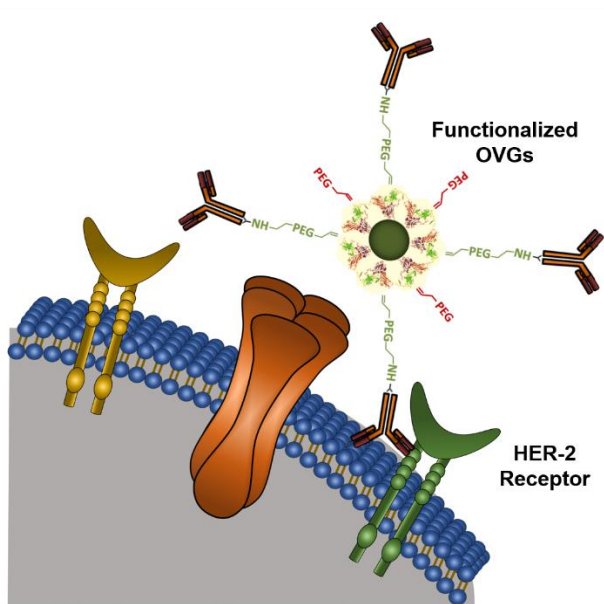


Figure 1 Schematic of specific cell-surface receptor targeting by functionalized OVGs.

2.2 EXPERIMENTAL SECTION

2.2.1 Reagents

Indocyanine green (Sigma Aldrich, St. Louis, MO) was dissolved in high purity deionized water at concentration of 645 μ M, and stored at -20 °C. Methoxy-poly(ethylene glycol)-butyraldehyde (PEG-ALD, MW=5,000 Da) and butyraldehyde-PEG-butylaldehyde (ALD-PEG-ALD, MW= 10,000 Da) (Laysan Bio Inc., Arab, AL) were stored at -20 °C in the absence of oxygen. The reducing agent, sodium dithionite ($\text{Na}_2\text{S}_2\text{O}_4$) (Sigma Aldrich, St. Louis, MO) was suspended to 20 nM an hour prior to its use. Anti-rabbit immunoglobulin G (IgG) (secondary antibody), Alkaline Phosphatase Conjugate (Promega, Madison, WI), 4', 6-diamidino-2-phenylindole (DAPI) (Invitrogen, Grand Island, NY) were used according to the manufacturer's suggestions. Rabbit monoclonal antibody against HER2 (Diagnostic Biosystems, Pleasanton, CA) was used as received.

2.2.2 Fabrication of OVGs

Barley was grown under greenhouse conditions with constant temperature and humidity. Once seedlings were 2-3 inches in height, we mechanically inoculated them with BMV stock diluted in water. The virus was allowed to propagate for several weeks until symptoms, as characterized by a mosaic, chlorosis and reddening of the hosts leaves, were observed in the second and third leaves of the plant (Figure S1). Similar to our previously reported methods (Figure 2) ^{24, 25}, OVGs were constructed using a four-step process: (1) virus purification from the systemically infected barley leaves; (2) virus disassembly and disassociation into capsid protein (CP) subunits; (3) separating the RNA

from CP subunits; and finally (4) doping the particle with ICG based on self-assembly.

Details of these steps are as follows:

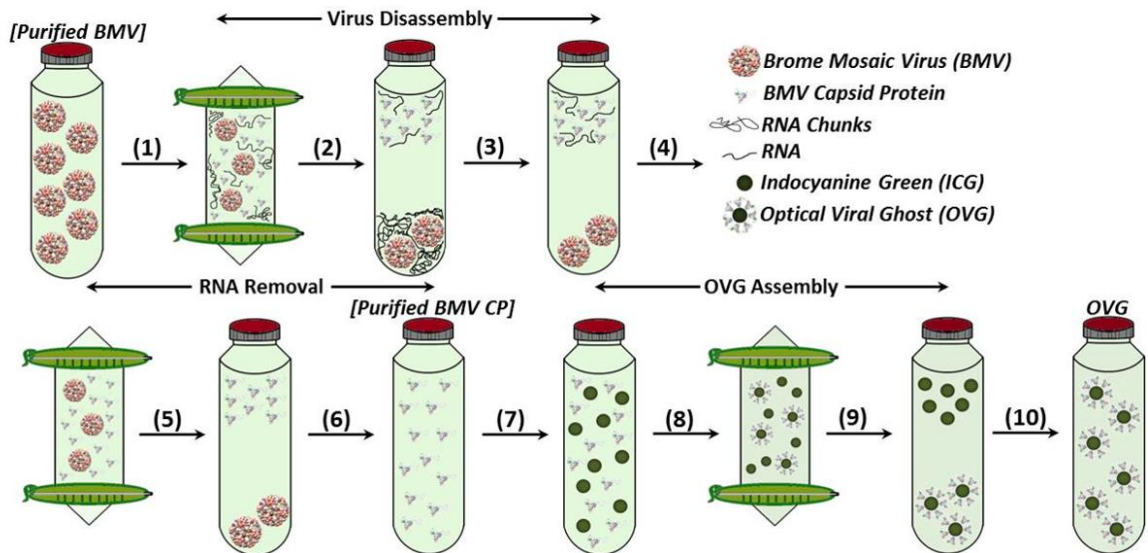


Figure 2 BMV dissociation, purification and self-assembly of OVGs. OVG fabrication from purified BMV. (1) Dialyze the BMV virions against disassembly buffer (24 hours); (2) centrifuge at low-speed ($\approx 18,200 \times g$ (relative centrifugal force (RCF)) (30 minutes) to remove un-dissociated BMV and large RNA chunks; (3) remove un-dissociated BMV particles by high-speed centrifugation ($\approx 262,000 \times g$ RCF, one hour) and collect supernatant containing dissociated capsid proteins (CP); (4) dialyze against pH=7.2 RNA re-assembly buffer to remove residual RNA; (5) discard pellet containing reassembled BMV by high-speed centrifugation ($\approx 262,000 \times g$ RCF, one hour); (6) collect supernatant containing purified dissociated BMV CP; (7) add ICG to the solution at specified ϕ -ratio (concentration of CP to that of ICG); (8) dialyze against BMV assembly buffer (24 hours) to assemble virus-like-particles; (9) remove excess ICG and dissociated CP by high-speed centrifugation ($\approx 262,000 \times g$ RCF, one hour), and keep the pellet containing intact OVGs; (10) re-suspend OVGs in BMV suspension buffer solution.

2.2.2.1 Virus purification

We collected BMV-infected barley leaves, and grinded them thoroughly using extraction buffer (0.5 M NaAc, 0.08 M MgAc, pH4). The extract was centrifuged in chloroform at $\approx 13,200 \times g$ (relative centrifugal force (RCF)) for 15 minutes at 4 °C. This process results

in formation of two distinct phases: a dark phase consisting of chloroform and heavy plant material, and a light phase consisting of extraction buffer and most plant proteins. We extracted the light phase, and added 10% sucrose solution (weight by volume) at a 1:8 ratio and subsequently centrifuged at $\approx 70,400 \times g$ RCF for three hours. The pellet was suspended in 2 ml of BMV suspension buffer consisting of the diluted extraction buffer in sterile distilled water in 1:10 ratio. Partially purified virus was subject to 25% sucrose density gradient centrifugation, and final concentration of the virus was determined from the absorbance value at 280 nm as measured by a spectrophotometer. Alternative methods for the purification of BMV virions are available, they make use of ultrafiltration and do not require ultracentrifugation decreasing time and cost of purification ⁴⁹.

2.2.2.2 Virus disassembly

The purified virus solution was dialyzed against disassembly buffer (1 L, 0.5 M CaCl₂, 50 mM Tris-HCl, 1 mM EDTA, 1 mM Dithiothreitol (DTT), 0.5 mM Phenylmethylsulfonyl Fluoride (PMSF), pH7.5) for 12 hours at 4 °C, resulting in an opaque precipitate made of condensed RNAs (step 1 in Figure 2). We collected the solution from the dialysis bag and centrifuged it at $\approx 18,200 \times g$ RCF for 40 minutes to pellet the viral RNA and non-dissociated BMV (step 2 in Figure 2). The supernatant was then centrifuged at $\approx 262,000 \times g$ RCF for one hour at 4°C to pellet any un-dissociated virus particles (step 3 in Figure 2).

2.2.2.3 Separating viral RNA from CP

CP subunits were dialyzed against 1 L RNA assembly buffer (50 mM NaCl, 50 mM Tris-HCl, 10 mM KCl, 5 mM MgCl₂, and 1 mM DTT, pH7.2) for 12 hours at 4°C (step 4 in Figure 2). It is this step during the procedure that ensures complete removal of the RNA during the synthesis of OVGs since RNA-containing virions will only form at the neutral pH. Therefore, the remaining CP subunits, not assembled into the virions, were completely separated from the RNA and did not contain any residual RNA. Solution was then collected and centrifuged at $\approx 262,000 \times g$ RCF for one hour to pellet RNA containing virions (step 5 in Figure 2). We collected the purified CP from the final supernatant (step 6 in Figure 2). The proteins can be used immediately or stored at 4 °C for 2-4 weeks. We assessed the purity of CP by examining its absorbance at 260 and 280 nm: a sample is considered to have high purity if the ratio of the absorbance at 260 to 280 nm is one or less⁵⁰. We note that the protocol to produce RNA-free BMV capsid protein subunits is well established and makes use of Northern and Western blots to verify in vitro assembly of wild type and RNA-depleted BMV^{51, 52}. We have previously confirmed the purity of the CP used in fabricating OVGs²⁴.

2.2.2.4 Capsid reassembly and ICG encapsulation

ICG was added to the solution (step 7 in Figure 2). CP subunits and ICG were then dialyzed against reassembly buffer (1 M NaCl, 50 mM NaAc, 1 mM EDTA, and 1 mM DTT, pH4.8) at 4 °C for 8 hours (step 8 in Figure 2). We collected the solution from the dialysis bag, centrifuged at $\approx 262,000 \times g$ RCF for one hour to pellet ICG-containing virions, and removed the supernatant (step 9 in Figure 2). BMV suspension buffer was added into the pellet, and the solution was stored overnight at 4 °C.

We define ϕ as the ratio of BMV CP concentration to that of ICG used during the OVG fabrication process. OVGs were prepared at ϕ values of 10 and 200, by fixing the ICG concentration at 5 $\mu\text{g/ml}$ while varying the CP concentration to 50 $\mu\text{g/ml}$ or 1,000 $\mu\text{g/ml}$ during the fabrication process. To increase the number concentration of OVGs (N_{OVG}), we carried two parallel fabrications, and combined the OVGs pellets obtained in step 9 of the fabrication process (Figure 2). The combined pellet was subsequently suspended in 1 ml of BMV buffer solution. This procedure effectively doubles N_{OVG} . All results, with the exception of those shown in Figure S3, were obtained using the two parallel fabrications procedure. We describe the methodology to estimate N_{OVG} in Supplemental Data section.

2.2.3 Functionalization of OVGs

Prior to functionalization of OVGs, we aimed to further increase N_{OVG} using ultra-centrifugal filter units (Millipore, Billerica, MA) with molecular weight cut-off (MWCO) of 100 kDa. It was essential to increase N_{OVG} due to considerable particle loss during the centrifugation steps involved in functionalization. Covalent attachment of anti-HER2 to the surface of OVGs was achieved by making use of the available amines on solvent accessible amino acid residues (e.g., lysine and arginine) on the CP subunits (Figure 3).

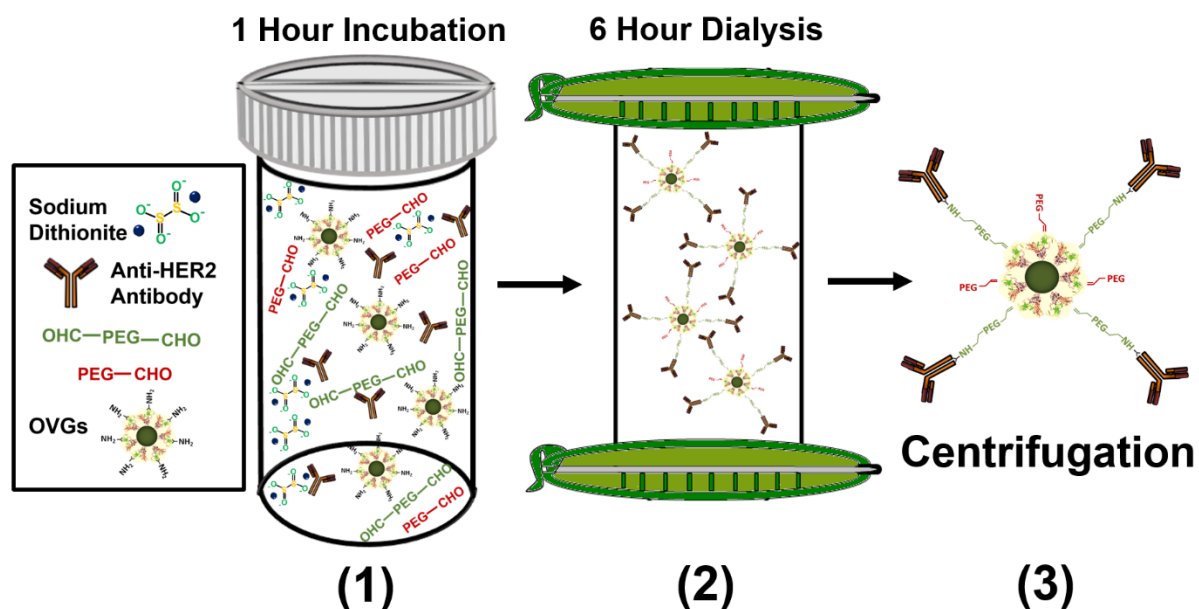


Figure 3 Surface functionalization of OVGs with anti-HER2 monoclonal antibody. (1) Equal number of single-aldehyde terminated (5 kDa), and double-aldehyde terminated (10 kDa) PEG polymers are added to OVGs in BMV suspension buffer followed by anti-HER2 monoclonal antibodies and 14 μ l of 20 mM sodium dithionite. The reaction is allowed to age for one hour at 4°C in dark. (2) Sample is subsequently dialyzed in OVG Suspension buffer for six hours using a 300 kDa MW-cutoff dialysis membrane. (3) After dialysis, sample is centrifuged to remove any unbound components, and recover functionalized OVGs.

Given the known molecular weights of each of the PEG chains (5 and 10 kDa for respective single- and double-aldehyde terminated PEG polymers), we determined the mass of each of the chain lengths to achieve a 1:1 number ratio during the fabrication process. The purpose of using the single-aldehyde terminated PEG is to reduce non-specific protein absorption to the surface of OVGs when used in vivo. The double-aldehyde terminated PEG serves as a linker between the surface of OVGs and the antibody. To the PEG mixture, we added 1 ml of concentrated OVG solution (with BMV

buffer as the solvent) followed by addition of 300 ng of the anti-HER2 antibody. After thorough mixing, we added 14 μ l of 20 mM sodium dithionite, and incubated the solution for one hour at 4 °C in the dark. After incubation, the sample was dialyzed using a filter with MWCO of 300 kDa (Spectra/Por, Rancho Dominguez, CA) (large enough for reducing agent as well as unbound antibody to be removed) against OVG suspension buffer (2 L) for six hours while replacing with fresh buffer every two hours. Functionalized OVGs were pelleted at $\approx 106,000 \times g$ RCF for three hours, and re-suspended in 1 ml of OVG suspension buffer.

2.2.4 Characterization of OVGs

The hydrodynamic diameters of OVGs and functionalized OVGs were measured by DLS. Absorption spectra in the range of 260-900 nm were obtained using a UV-VIS-NIR spectrophotometer (Cary 50, Varian Inc., Santa Clara, CA) with optical pathlength of 1 cm. NIR fluorescence spectra in response to photo-excitation at 680 nm with 450W xenon lamp were recorded in the 695-900 nm spectral range using a fluorescence spectrophotometer (Fluorolog-3, Horiba –Jobin-Yvon, Inc.). We chose 680 nm as the excitation wavelength based on the results of an excitation-emission map for free ICG at concentration of 8 μ M in BMV buffer solution (Figure S2), which showed that photo-excitation at 680 nm produced intense emissions in ≈ 690 -720 nm and 800-820 bands (Figure S2).

We normalized the emission intensity spectra as:

$$\zeta(\lambda) = \frac{F(\lambda)}{[1 - 10^{-A(\lambda_{\text{ex}})}]} \quad (1)$$

where $\zeta(\lambda)$ is the wavelength (λ) dependent normalized emission intensity, $F(\lambda)$ is the recorded emission intensity, and $A(\lambda_{\text{ex}})$ is the absorbance value at the excitation wavelength λ_{ex} .

2.2.5 Cell Lines and Fluorescence Microscopy

We used the SKOV-3 (ATCC[®], Manassas, VA) human ovarian cancer cell line, which has relatively high expression levels of the HER2 receptor⁵³. As control cells, we used the OVCAR-3 cell line (ATCC[®]), which have relatively low expressions of the HER2 receptor⁵⁴. Cells were cultured in Corning cell culture flasks containing Rosewell Park Memorial Institute (RPMI) 1640 medium supplemented with 1% Penicillin/Streptomycin, and 10% fetal bovine serum (ATCC[®]). They were allowed to reach 85% confluency before passaging. When imaging under a 40X objective, cells were passaged onto BD Falcon 12-well plates at a density of $\approx 2 \times 10^5$ cells/ml eight hours prior to imaging. When imaging under a 100X objective, cells were passaged eight hours prior to imaging onto a chambered cover glass at a density of $\approx 1 \times 10^5$ cells/ml.

In the first set of experiments, SKOV-3 and OVCAR-3 cells were incubated for 45 minutes at 4 °C with functionalized OVGs to minimize/prevent internalization of the nano-particles, which normally occurs at 37 °C. In the second set of experiments, SKOV-3 cells were incubated for one hour at physiological temperature (37 °C) with free ICG, OVGs, and functionalized OVGs. Wells were covered by aluminum foil to protect from ambient light. After incubation, cells were washed twice with fresh RPMI media, and maintained in phosphate buffer saline (PBS). Cells were then incubated for 20 minutes with DAPI, and subsequently, washed twice with fresh PBS and fluorescently imaged.

In a third experiment, SKOV-3 cells were incubated with functionalized OVGs for one hour at 37 °C. After incubation cells were stained with DAPI, washed and subsequently incubated for two hours with a fluorescently-labeled secondary antibody (anti-rabbit-FITC) specific for the anti-HER2 monoclonal antibody functionalized on the surface of OVGs. After incubation, cells were washed twice and re-suspended in PBS.

Finally, in a fourth set of experiments, mixed populations of both OVCAR-3 and SKOV-3 cells were incubated with either OVGs, or the functionalized OVGs. SKOV-3 and OVCAR-3 cells were seeded at \approx 20,000 and 40,000 per well, respectively, and allowed to grow for 36 hours. Subsequently, we added 1.5 ml of growth medium, and 50 μ l of solution containing OVGs or functionalized OVGs to a petri dish containing the mixed population of OVCAR-3 and SKOV-3 cells. The absorbance values of OVGs and the functionalized OVGs at 780 nm were equivalent to that of 20 μ M ICG dissolved in BMV suspension buffer at the same wavelength. Cells were incubated for 30 minutes at 37 °C, and then thoroughly washed three times using PBS. Following the last wash, cells were incubated with 300 μ l of a 300 nM DAPI solution for 15 minutes.

Fluorescent images of the cells in all experiments were acquired in response to photo-excitation at 740 ± 35 nm. Images were collected using an electron multiplier (EM) gained CCD camera (QuantEMCCD, Hamamatsu, Bridgewater, NJ) in combination with a long pass emission filter (>770 nm). Camera exposure time was set at 0.1 s in all imaging sessions. The contrast and brightness for all fluorescent images were normalized to the levels of cells incubated with functionalized OVGs. In the case of Figure 7 where

two cells lines were used, signal was normalized to the SKOV-3 cell line incubated with functionalized OVGs. We used the ImageJ software to analyze the images.

2.2.6 Flow Cytometry

Cells in culture were seeded onto a 12-well plate at a concentration of $\approx 1 \times 10^6$ cells/ml one hour before the experiment to prevent attachment to the plate. SKOV-3 and OVCAR-3 cells were incubated between 45 minutes to one hour at 37 °C with OVG suspension buffer, free ICG, OVGs, and functionalized OVGs. To validate specificity, we performed a competitive binding assay where SKOV-3 cells were simultaneously incubated with functionalized OVGs, and either 300 ng or 1.2 μ g of competing anti-HER2 antibody. After incubation, we washed the cells twice with PBS prior to flow cytometry by centrifuging at 290 x g RCF for 4 minutes, and re-suspending them in PBS. All cells were maintained in suspension during the experiment. Propidium iodide was then added to identify any apoptotic or dead cells. A flow cytometer (BD FACSAria cell sorter, San Jose, CA) with photo-excitation at 663 nm and emission collection at >785 nm for ICG signal detection was used to determine the interaction of the OVG suspension buffer, ICG, OVGs, and functionalized OVGs with the SKOV-3 and OVCAR-3 cell lines. All studies were done in triplicates. During flow cytometry, a minimum of 50,000 events were counted for each triplicate.

2.3 RESULTS AND DISCUSSION

2.3.1 Characterization of OVGs

Free ICG dissolved in BMV suspension buffer at a concentration of 13 μ M has maximum absorption at 780 nm, attributed to the monomeric form of ICG (Figure 4a). This

maximum absorption is consistent with the dominant monomeric absorption peak of ICG dissolved in deionized water at dilute concentrations ($\approx < 14 \mu\text{M}$)¹³. A secondary absorption peak at 700 nm for free ICG is attributed to its H-like aggregate forms^{13,25}.

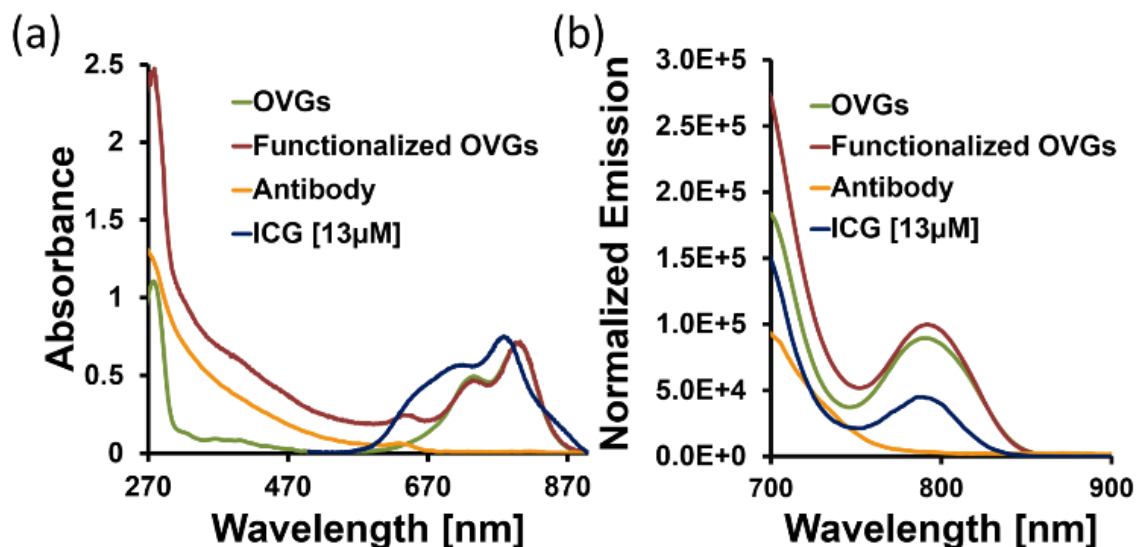


Figure 4 (a) Absorption, and (b) normalized fluorescence emission spectra of non-functionalized OVGs, anti-HER2-functionalized OVGs, anti-HER2 monoclonal antibody (300 ng/ml), and 13 μM ICG in response to photo-excitation at 680 nm. Solvent was OVG suspension buffer in all cases. The ϕ -value used to fabricate both non-functionalized and functionalized OVGs was 200.

Non-functionalized and anti-HER2-functionalized OVGs have nearly identical absorption in the 700-900 nm spectral band, which includes the range for ICG absorption (Figure 4a). This result suggests that there was no ICG loss or degradation of particles due to the surface functionalization process. The spectral peaks at 735 nm and 795 nm are associated with the H-like aggregate and monomeric forms of ICG⁵⁵, respectively, and remain unaltered with functionalization of OVGs. We attribute the bathochromic shifts in the absorption peaks of the monomeric and H-like aggregates of ICG within to OVGs to

the binding of ICG monomers and H-like aggregates to the CP subunits. In accordance with the excitation theory for molecular aggregation⁵⁶, the excitonic states of the bound ICG can split into two levels, E' and E'' . The lower excited state, E' , involves a linear “head-to-tail” arrangement of the transition dipole moments of the CP-bound forms of the ICG. Photo-excitation of these bound complexes produces a transition from the ground state to E' (the lower of the two excited levels), and therefore, a bathochromic shift.

We attribute the absorption of non-functionalized and anti-HER2-functionalized OVGs at 280 nm to the tyrosine, tryptophan, and cysteine residues in the CP^{50, 57}. Absorbance value at 280 nm increased from ≈ 1.1 for the antibody to ≈ 2.4 for functionalized OVGs. The absorption of the antibody in the 630-660 nm range is due to the manufacturing impurities. The characteristically flat absorption spectrum for the OVGs between 310-670 nm changes to a wavelength-dependent spectrum after the conjugation with the antibody. The spectrum for functionalized OVGs in the aforementioned range is a superposition of the antibody and OVG spectra, suggesting that most of the antibody was grafted onto the OVGs. The increased absorbance values for functionalized OVGs in the range of 270-700 nm are attributed to successful grafting of the antibody. The difference in absorbance value of functionalized OVGs and non-functionalized OVGs at 280 nm matches the absorbance value of the antibody at this wavelength, another indication that nearly all the antibody was successfully used in the conjugation process.

The fluorescence emission peaks of free ICG at 700 nm and 790 nm are attributed to its H-like aggregate and monomeric forms, respectively (Figure 4b). While the shapes

of the fluorescence emission spectra for OVGs and functionalized OVGs are similar, there is increased intensity associated with the H-like form of ICG at 700 nm for the functionalized OVGs. This increased emission intensity includes an emission contribution from the antibody due to its impurities. The normalized emission for both non-functionalized and functionalized OVGs at 790 nm are about a factor of two higher than that of free ICG, indicating the presence of monomeric forms of ICG within the OVGs.

Immunohistochemical staining assay was used to further validate the successful conjugation of OVGs with anti-HER2. After incubation with nitroblue tetrazolium (NBT) and the alkaline phosphatase substrate 5-bromo- 4-chloro-3-indolyl phosphate (BCIP), there were no color changes in the cases of suspension buffer (negative control) and non-functionalized OVGs. However, we observed a change to dark purple in the case of functionalized OVGs and free antibody in suspension (positive control) (Figure S3).

The estimated mean and standard deviation (SD) values of peak diameter of wild type BMV and non-functionalized OVGs were 25.4 ± 2.9 and $24 \text{ nm} \pm 3$, respectively (Figure 5), and consistent with our previously reported results²⁴. Upon conjugation with anti-HER2, the estimated mean \pm SD values of peak diameter of functionalized OVGs became approximately 37.5 ± 3.6 nm, respectively (Figure 5).

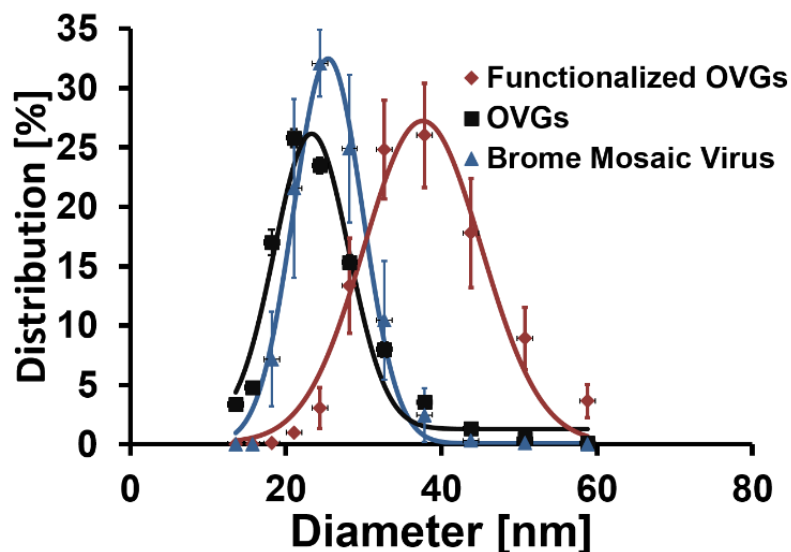


Figure 5 Diameter distributions of non-functionalized OVG, anti-HER2-functionalized OVGs, and wild type BMV as determined by dynamic light scattering. We present the mean of three measurements on three identically prepared samples with error bars representing the standard deviations from the mean. We fitted Lorentzian functions to the measured diameter distributions (solid curves). The ϕ -value used to fabricate both non-functionalized and functionalized OVGs was 200.

We have previously reported on the physical stability of OVGs. Specifically, OVGs remained intact after 11 days of storage at 4 °C in BMV suspension buffer, as evidenced by TEM imaging ²⁴. OVGs at 11 days post-construction had a diameter of 23.3 ± 3 nm (mean \pm SD), nearly identical to the values immediately after synthesis (24.3 ± 3.9 nm) ²⁴. In another study, we demonstrated that OVGs remained intact, and did not disassociate when incubated with cell culture medium (McCoy's 5A) containing 5% fetal bovine serum (FBS) at physiologically-relevant pH (7.4) and stored in dark at 4 °C for at 24 hours ²⁵. We attributed this stability to the low ionic strength of the cell culture medium (0.13 mol/l) despite the physiological pH of the incubation medium.

Additionally, our spectral recordings indicated that the absorption and fluorescence characteristics of OVGs were retained after 79 days of storage in these conditions in a cell culture medium containing 10% FBS²⁵.

2.3.2 OVG Functionalization and Specificity for HER2

Based on fluorescence imaging, NIR emission was detected from SKOV-3 cells incubated with anti-HER2-functionalized OVGs for two hours at 37 °C (Figure 6). We also observed co-localization of fluorescence signals from the FITC-labelled secondary antibody bound to anti-HER2 monoclonal rabbit antibodies conjugated to the surface of OVGs. To further examine the specificity of functionalized OVGs in targeted molecular imaging of HER2 expression on SKOV-3 cells, we incubated SKOV-3 cells for one hour at 37°C with free ICG (negative control), non-functionalized OVGs (positive control), and anti-HER2-functionalized OVGs. There was none or minimal NIR fluorescence emission from SKOV-3 cells incubated with free ICG or non-functionalized OVGs. However, incubation with functionalized OVGs resulted in considerable NIR fluorescence emission from these cells (Figure 7a (iii)).

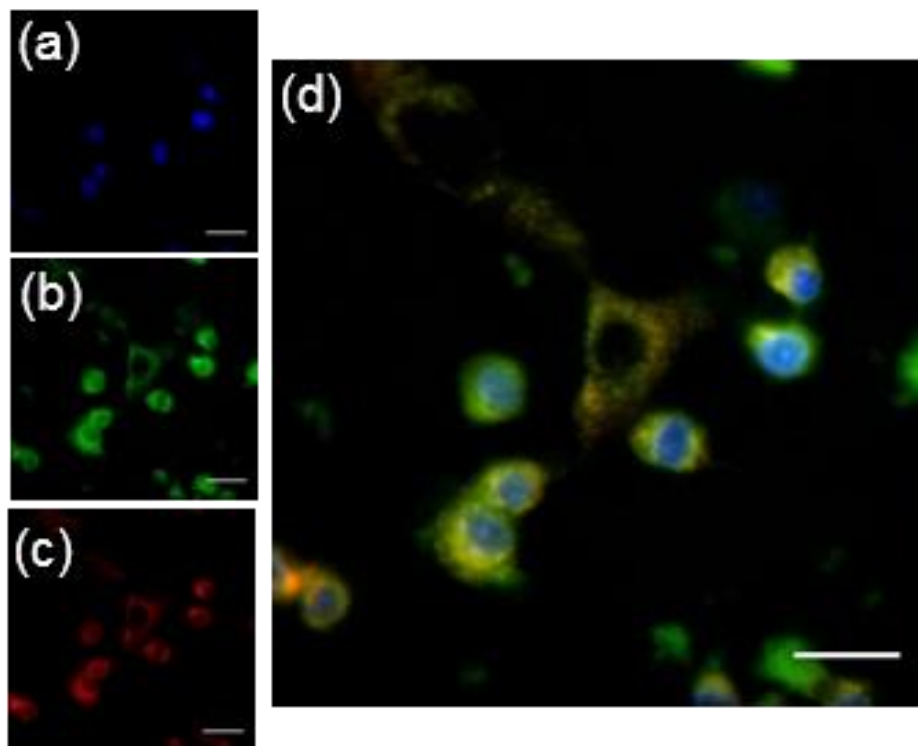


Figure 6 Fluorescence image of SKOV-3 cell line after two hours of incubation with anti-HER2-functionalized OVGs. Individual panels show: (a) DAPI-stained cell nuclei (blue), (b) FITC-labeled secondary antibody (green), (c) anti-HER2-functionalized OVGs (red), and (d) merged images. Scale bars correspond to 20 μm . The ϕ -value used to fabricate both non-functionalized and functionalized OVGs was 10.

We performed additional studies to further validate the capability of functionalized OVGs in targeted molecular imaging of HER2 receptors. Specifically, we used the OVCAR-3 cells, which have relatively low expression of the HER2 receptor as control cells. Both SKOV-3 and OVCAR-3 cells were incubated for 45 minutes with anti-HER2-functionalized OVGs at 4 $^{\circ}\text{C}$ to minimize internalization of the particles that normally occurs at physiological temperature^{58, 59}. NIR Fluorescent images demonstrated greater emission from the membrane of SKOV-3 cells, delineated by the bright rim

(falsely-colored in red), as compared with OVCAR-3 cells, indicating the specific binding of the functionalized OVGs to the HER2 receptors over-expressed on the SKOV-3 cells (Figure 7b).

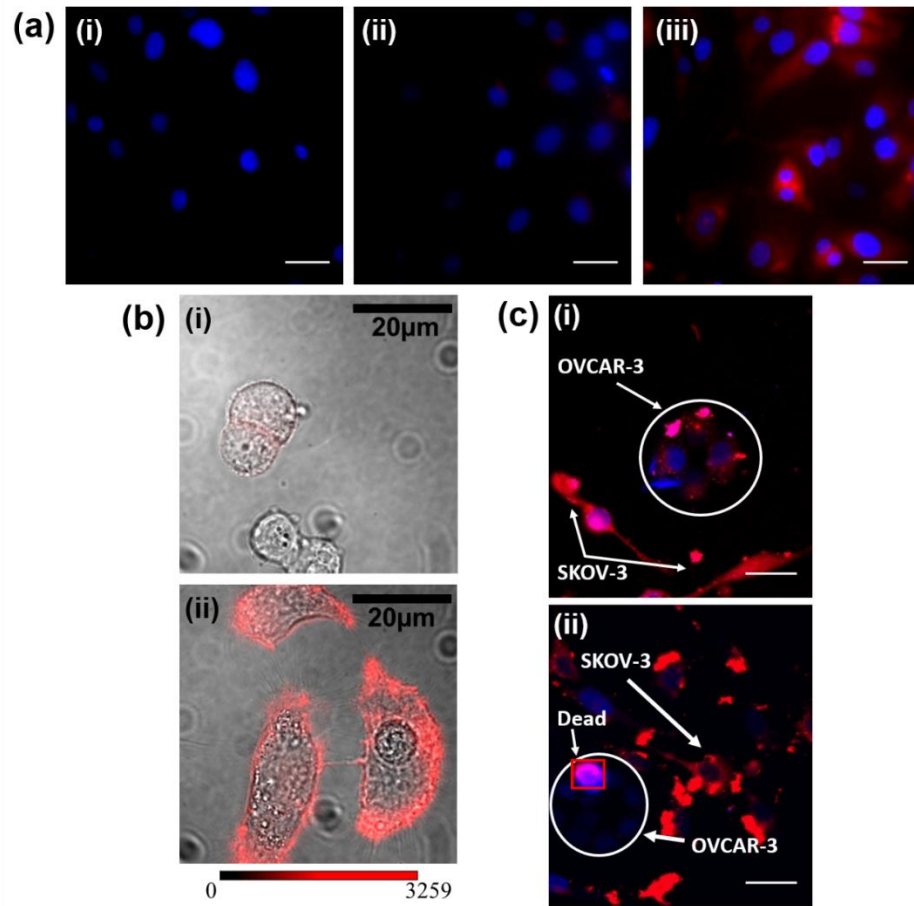


Figure 7 Fluorescent images of (a) SKOV-3 cells following one hour of incubation at 37 °C with (i) free ICG, (ii) non-functionalized OVGs, and (ii) anti-HER2-functionalized OVGs. (b) Merged bright-field and NIR fluorescence images of (i) OVCAR-3, and (ii) SKOV-3 cell lines incubated with functionalized OVGs for 45 minutes at 4 °C.. (c) NIR fluorescence images of co-cultures of OVCAR-3 and SKOV-3 cell populations after 30 minutes of incubation at 37 °C with (i) OVGs, and (ii) functionalized OVGs. The boxed region in panel (c(ii)) points to a dead OVCAR-3 cell. For both (a) and (b) the ϕ -value used to fabricate both non-functionalized and functionalized OVGs was 10 and 200 in (c). Blue false-colour indicates the presence of DAPI while the red false-colour indicates NIR emission. All scale bars correspond to 20 μm.

Finally, we incubated co-cultures of OVCAR-3 and SKOV-3 cells with OVGs (Figure 7c (i)), and functionalized OVGs (Figure 7c (ii)) at 37 °C to further evaluate the specificity of functionalized OVGs in targeted imaging of the HER2 receptor over-expression on SKOV-3 cells. When incubating with OVGs, the fluorescence emissions levels were comparable between the two cell lines (Figures 7c (i)). However, when incubating the co-cultures of OVCAR-3 and SKOV-3 cells with functionalized OVGs, only the SKOV-3 cells could be fluorescently imaged (Figure 7c (ii)), indicating the effectiveness of the functionalized OVGs in specific imaging of HER2 receptor over-expression on SKOV-3 cells.

2.3.3 Quantification of HER2 Targeting

We used flow cytometry to quantify the targeting of HER2 by the various reagents (Figure 8). Specifically, we determined the relative fraction of the population of SKOV-3 or OVCAR-3 cells (N) that emitted NIR fluorescence (> 785 nm) due to ICG (data on the actual number of cells exhibiting ICG fluorescence signal are provided in (Figure S4)). The value of N for SKOV-3 and OVCAR-3 cells incubated with OVG suspension buffer (negative control), free ICG (positive control), or non-functionalized OVGs for 45 minutes at 4 °C, were significantly lower than those cells incubated with anti-HER2-functionalized OVGs (Figure 8a). There was also a statistically significant increase in N for SKOV-3 cells following incubation with anti-HER2-functionalized OVGs as compared with OVCAR-3 cells, further validating the effectiveness of the functionalized particles in specific targeting of the HER2 over-expression on SKOV-3 cells.

We also performed competitive binding assay experiments in which SKOV-3 cells were incubated at 37 °C with anti-HER2-functionalized OVGs alone, or in the presence of the free antibody for two hours. The N of SKOV-3 cells that could be targeted with anti-HER2-functionalized OVGs, and emit NIR signal, progressively became lower with increasing amount of the free antibody (Figure 8b). In the presence of 1.2 μ g of the antibody, the N of SKOV-3 cells that emitted NIR signal approached the value when the cells were incubated with free ICG. Therefore, the results of these experiments further confirm that the functionalized antibody were effective in specific binding to the HER2 receptors on SKOV-3 cells, and the binding was reduced in the presence of a competing antibody.

The effectiveness of using fluorescein isothiocyanate (FITC) (a visible optical tracer with peak emission at 520 nm when photo-excited at 495 nm), conjugated with folate hapten, for targeted real time optical imaging of the folate receptor- α over-expression, was demonstrated for the first time in women with ovarian cancer ⁶⁰. Disseminated peritoneal tumor deposits with resolution of \approx 1 mm could be visualized. Despite the use of non-NIR wavelengths, this study demonstrated that molecularly-targeted intraoperative fluorescence imaging of intraperitoneal tumors in humans is feasible, and provides a potentially effective approach for detection of disseminated nodules that cannot be currently identified by existing methods.

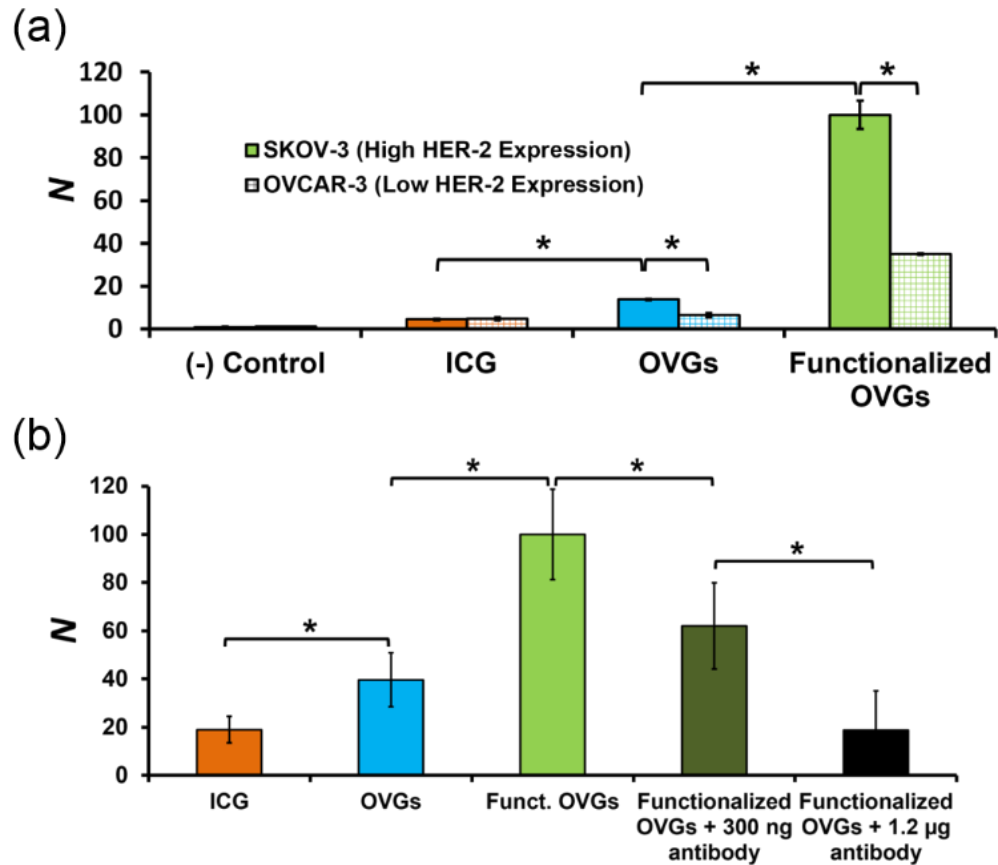


Figure 8 Quantification of HER2 targeting by flow cytometry. (a) The relative mean fraction of the populations (N) of SKOV-3 and OVCAR-3 cells emitting NIR fluorescence signal after 45 minutes of incubation at 4°C with suspension buffer (negative control), ICG (positive control), OVGs, and functionalized OVGs. **(b)** The relative mean fraction of the populations (N) of SKOV-3 cells emitting NIR fluorescence after incubation for two hours at 37 C with ICG, OVGs, and anti-HER2-functionalized OVGs. Incubation with functionalized OVGs was performed in the absence, or presence of 300 ng or 1.2 μg of anti-HER2 antibody. Error bars represent the standard deviations from the mean for triplicate samples. Asterisks represent statistically significant differences between the indicated pairs (p-value < 0.05). The φ value used to fabricate both non-functionalized and functionalized OVGs was 10.

Kosaka et al. have demonstrated the endoscopic NIR imaging of peritoneal ovarian cancer nodules in mice using ICG ⁶¹. The ability to image tumors by ICG, in the

absence of molecular targeting moieties, was presumably due to binding of ICG to plasma proteins, resulting a macromolecule-like structure that would accumulate in tumors via the enhanced permeability and retention (EPR) effect ⁶². Other NIR fluorophores, including Cy5.5 and alexaFlour680 conjugated to a cyclic peptide and targeting the $\alpha 3$ integrin ⁶³, NHS-IR800 conjugated to Bevacizumab to target the vascular endothelial growth factor or conjugated to Trastuzumab to target HER2 ⁶⁴, and 1,1'-dioctadecyl-3,3,3',3'-tetramethylindo-tricarbocyanine iodide bis-oleate (DiR-BOA) conjugated to folate to target the folate receptor- α have been reported ⁶⁵.

Our group has previously reported on the use of synthetic polymer-based nanoconstructs composed of poly(allylamine) hydrochloride chains cross-linked ionically with sodium phosphate, and doped with ICG for imaging of ovarian cancer cells ²². In comparison with those polymeric constructs, OVGs are highly monodispersed and consistently self-assemble into vehicles at room temperature with diameter distribution in the range of 20-28 nm without the need use of any additional procedures to improve size uniformity ²⁴. Diameter of the fabricated polymeric constructs can range between \approx 50-110 nm during a single procedure ²¹. Formation of mono-dispersed polymeric constructs requires appropriate charge ratios of the polymer to salt, curing time, dilution, and low temperature (6 °C) ⁶⁶. While ICG loading efficiency of nearly 100% can be achieved with OVGs ²⁴, the loading efficiency into the synthetic polymer-based constructs ranges between \approx 36-52% ⁶⁶.

Nano-complexes consisting of a silica core surrounded by a gold nanoshell, and doped with ICG and superparamagnetic iron oxide, for dual NIR and MRI imaging of

ovarian cancer cells in vitro have been reported ⁶⁷. To achieve HER2 binding capability, the surface of these constructs was modified by attachment of streptavidin, which served as the binding site for biotinylated anti-HER2 rabbit antibody. Functionalized OVGs provide a simpler structural system since the inherent presence of the amines on the surface of the particles provide addressable sites for covalent attachment of various targeting moieties including the anti-HER2 antibody, without the need for additional attachment of other molecules such as streptavidin.

To the best of our knowledge, this is the first study to demonstrate the utility of a plant-virus derived optical nano-construct for targeted NIR molecular imaging of ovarian cancer biomarker receptors. Constructs derived from replication deficient plant viruses are especially attractive since plant viruses do not infect humans ²⁷, and constructs containing plant virus components are expected to be biocompatible and biodegradable in mammalian systems ²⁸⁻³⁰. Our preliminary findings demonstrate the absence of an acute immunogenic response in mice injected with a single dose of 100 µg of purified CP proteins ⁶⁸. Additionally, such constructs provide naturally available chemical functional groups on their surfaces as addressable sites for functionalization ⁶⁹, and can be produced in large quantities ⁷⁰.

While we have focused on functionalization of OVGs with anti-HER2 in this study, OVGs can potentially be functionalized with an array of targeting moieties with potential for imaging various cancer types. Our future works will include studies to investigate the effectiveness of functionalized OVGs in targeted NIR imaging of ovarian tumors in animal models.

2.4 CONCLUSIONS

In this study, we present the first results that demonstrate successful functionalization of OVGs with anti-HER2. Using fluorescence imaging and flow cytometry, we show the effectiveness of these functionalized OVGs for targeted NIR imaging of ovarian cancer cells with over-expressed HER2 receptors. These virus-resembling nano-constructs could help improve the clinical management of ovarian cancer by providing the capability for detection and imaging of otherwise undetectable nodules when used in conjunction with open surgical procedures.

2.5 SUPPLEMENTAL INFORMATION

2.5.1 Virus propagation

Barley leaves are mechanically inoculated with brome mosaic virus (BMV) in water. Infected barley leaf stocks are stored at -80°C to prevent protein degradation, and increase storage time. When frozen stocks are almost depleted, we begin a new cycle of viral propagation by seeding barley in sterile soil and watering with fertilizer-doped water. By day seven, the seedlings are roughly 2-3 inches tall, and have grown a single leaf 2-3 inches in height. On this day, we mechanically disrupt the leaves by using carborundum as an abrasive to help break the leaves surface, and daub the leaves with the BMV suspension. For best results, we infect young plants, as symptoms are not apparent in older plants. By day 15 after infection, a secondary leaf has formed and presents symptoms. Usually the primary leaf lacks symptoms, and eventually dies off while the plant continues to grow. It is only in the secondary leaf and tertiary leaf, usually seen by

day 21, that the mosaic pattern is apparent. Apart from the mosaic, infected seedlings will grow much slower than healthy ones. These symptoms allow us to choose only seedlings that are successfully infected.

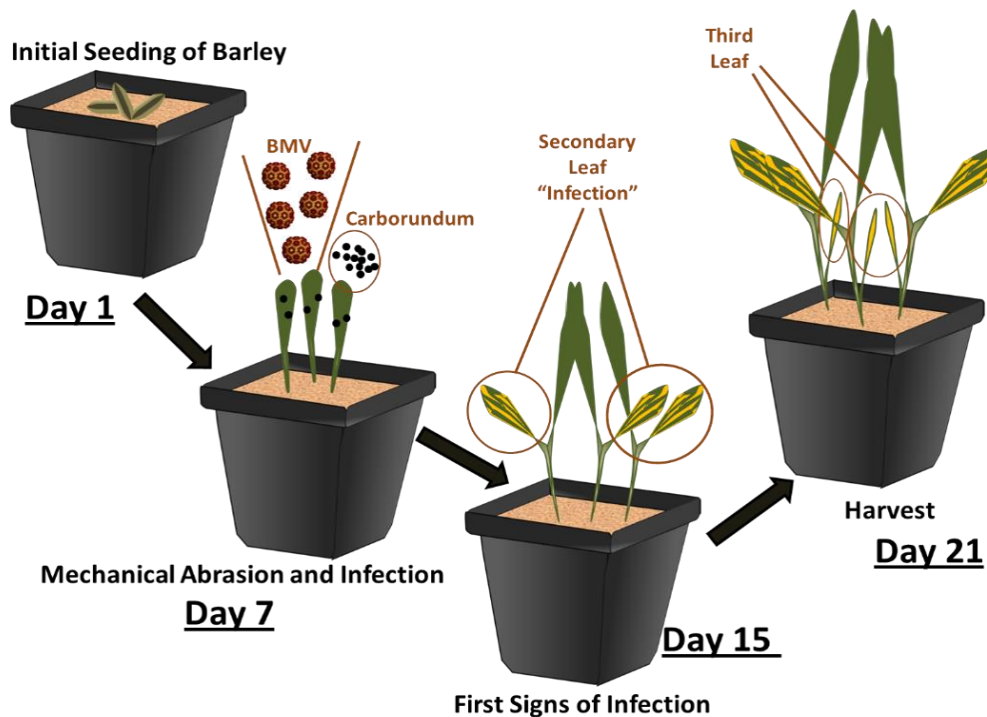


Figure 9 Barley is seeded at day one in sterile nutrient rich soil, and placed in a controlled green house. At day seven, the seedling is between 2-3 inches in height at which point the single leaf is mechanically disturbed with the use of carborundum, and the virus is introduced directly into the cell. By day 15, signs of infection begin to appear in the form of a brome mosaic pattern. By week three, depending on the degree of infection, the plants are ready for collection.

2.5.2 Selection of ICG concentration for encapsulation into optical viral ghosts (OVGs), and photo-excitation wavelength

We acquired the fluorescence emission spectra of 2-40 μM ICG dissolved in OVG suspension buffer. The respective peak emission intensity values, associated with the monomeric and H-like forms of ICG at 790 and 700 nm, as a function of ICG

concentration dissolved in OVG suspension buffer are presented in Figure S2(a). Maximum emissions at 790 and 700 nm corresponded to ICG concentrations of 10 and 8 μM , respectively. Using 8 and 10 μM ICG as initial test concentrations for encapsulation into OVGs, we subsequently determined that ICG concentration of 6.5 μM (corresponding to 5 μg of ICG dissolved in 1 ml of OVG suspension buffer) produced comparable integrated emission to that of free ICG at a similar concentration. Therefore, we proceeded with use of 6.5 μM ICG to fabricate the OVGs.

To select an appropriate photo-excitation wavelength, we obtained the excitation-emission map for 8 μM ICG dissolved in OVG suspension buffer (Figure S2(b)). Photo-excitation at 680 nm produced intense emissions in $\approx 690\text{-}720$ nm and $800\text{-}820$ nm bands. Maps for OVGs fabricated using 6.5 μM ICG were nearly identical.

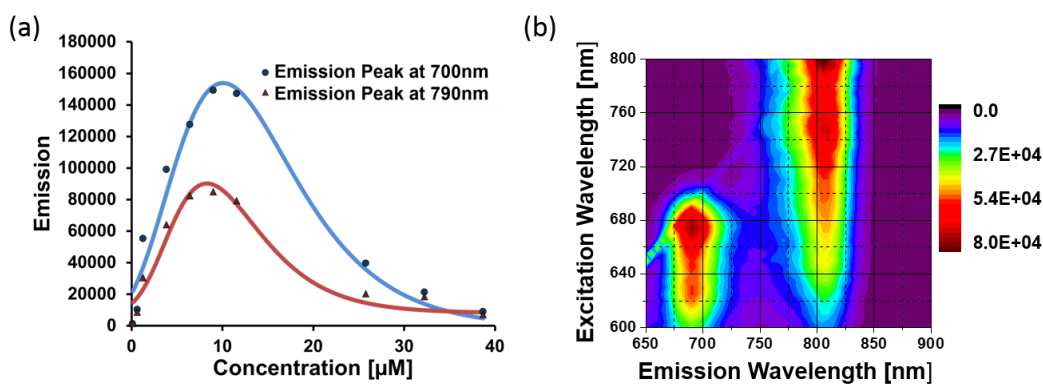


Figure 10 (a) Concentration-dependent fluorescence emission intensities of ICG at 700 and 790 nm, corresponding to H-Like and monomeric forms of ICG, respectively. Solvent was OVG suspension buffer. We fitted the measured spectra with Lorentzian distribution functions. (b) Excitation-emission map for 8 μM free ICG dissolved in OVG suspension buffer.

2.5.3 Estimating the number of OVGs

Using the absorbance of OVGs at 280 nm, we estimate the capsid protein (CP) concentration, and subsequently the number of OVGs fabricated at a given value of ϕ , defined as the ratio of CP concentration ($C_{\text{CP-fabrication}}$) to that of ICG ($C_{\text{ICG-fabrication}}$) used in fabricating the OVGs. We fixed $C_{\text{ICG-fabrication}}$ to $5 \mu\text{g}\cdot\text{mL}^{-1}$, but varied $C_{\text{CP-fabrication}}$ to $1,000 \mu\text{g}\cdot\text{mL}^{-1}$ and $50 \mu\text{g}\cdot\text{mL}^{-1}$ to fabricate OVGs at $\phi = 200$ and 10 .

Considering that the absorbance (A) (unitless) of a molecule is

$$A = \varepsilon Cl \quad (1)$$

we express the concentration (C) ($\text{moles}\cdot\text{L}^{-1}$) of the CP as:

$$C = \frac{A}{\varepsilon l} \quad (2),$$

where ε is the molar extinction coefficient ($\text{L}\cdot\text{mol}^{-1}\cdot\text{cm}^{-1}$), and l is the pathlength (1 cm in this case).

Value of ε for the CP is the sum of the contributions from the major amino acids responsible for most of the absorption:^{71, 72}

$$\varepsilon = (5,690n_1\text{Trp} + 1,280n_2\text{Tyr} + 120n_3\text{Cys}) = 23,590\text{L}\cdot\text{mol}^{-1}\cdot\text{cm}^{-1} \quad (3)$$

where n_1 , n_2 , and n_3 correspond to the number of tryptophan (Trp), tyrosine (Tyr) and cystines (Cys) residues, respectively. These numbers are: $n_1=3$, $n_2=5$, and $n_3=1$. The values 5,690, 1,280, and 120, respectively, correspond to the extinction coefficients of Trp, Tyr, and Cys at 280 nm⁷¹ and have units of $\text{L}\cdot\text{mol}^{-1}\cdot\text{cm}^{-1}$.

Based on the molecular weight of a single subunit of BMV CP (MW_{BMV_CP}) (20,385 Da \approx 3.39×10^{-17} mg),⁷³ we express the concentration of CP in $\text{mg} \cdot \text{ml}^{-1}$ as:

$$C = \left(\frac{A}{\varepsilon} \right) * MW_{BMV_CP} = \left(\frac{A}{23,590} \right) * 20,385 \quad (4)$$

Therefore, by using equation (4) in conjunction with measured value of A at 280 nm, we can determine C of the CP, and subsequently the desired $C_{CP\text{-fabrication}}$. Specifically, $A=1.16$ corresponds to $1.0 \text{ mg} \cdot \text{mL}^{-1}$ of CP. To obtain $C_{CP\text{-fabrication}} = 1 \text{ mg} \cdot \text{mL}^{-1}$, we dilute the CP stock solution stored at concentration of $3 \text{ mg} \cdot \text{mL}^{-1}$.

While wild type BMV has 180 CP subunits, corresponding to $T=3$ triangulation,⁷⁴ genome free CP of BMV assemble into T-like triangulations structures with 60 subunits.^{24, 75} Therefore, we estimate the mass (M) of a single OVG as:

$$M_{OVG} = 60 * (3.39 * 10^{-17} \text{ mg}) = 2.03 * 10^{-15} \text{ mg} \quad (5)$$

Subsequently, the number of OVGs (N_{OVG}) can be determined from the mass of the CP subunits utilized during the fabrication of OVGs and the mass of a single OVG:

$$N_{OVG} = \frac{M_{CP\text{-fabrication}}}{M_{OVG}} \quad (6)$$

For $M_{CP\text{-fabrication}} = 1 \text{ mg}$ (based on $C_{CP\text{-fabrication}} = 1 \text{ mg} \cdot \text{mL}^{-1}$ and 1 mL reaction volume), resulting in $\phi = 200$, and $M_{OVG} = 2.03 \times 10^{-15} \text{ mg}$, we determine N_{OVG} to be 4.95×10^{14} in 1 mL. This number is on the same order (10^{14}) as that reported for similar protein concentrations and nanoparticles diameter.⁷⁶ For $\phi = 10$, we determine N_{OVG} to be 2.475×10^{13} in 1 mL.

These estimated values of N_{OVG} correspond to a single OVG fabrication process. For n parallel fabrications where the resulting pellets are combined and re-suspended in 1 ml of BMV buffer solution (as described in the main text of the manuscript), the resulting number of OVGs will be $n \times N_{OVG}$ in 1 mL. For example, for $n = 2$ (i.e., two parallel fabrications), $N_{OVG} \approx 9.9 \times 10^{14}$ per 1 mL when $\phi = 200$.

2.5.4 Estimating the number of ICG per OVG

We first determine the number of ICG molecules used during the fabrication process ($N_{ICG-fabrication}$) as:

$$N_{ICG-fabrication} = M_{ICG-fabrication} \cdot \frac{N_A}{MW_{ICG}} \quad (7)$$

where N_A is the Avogadro's Number ($6.022 \times 10^{23} \text{ mole}^{-1}$), and MW_{ICG} is the molecular weight of ICG ($774.97 \text{ g} \cdot \text{mole}^{-1}$). With $M_{ICG-fabrication} = 5 \text{ } \mu\text{g}$ (based on the use of $5 \text{ } \mu\text{g/ml}$ of ICG and 1 mL of reaction volume), we determine $N_{ICG-fabrication} = 3.87 \times 10^{15}$. Finally, we determine $N_{ICG-OVG}$, the average number of ICG molecules in an OVG, as:

$$N_{ICG-OVG} = \frac{N_{ICG-fabrication}}{N_{OVG}} \quad (8)$$

With $N_{ICG-fabrication} = 3.87 \times 10^{15}$, and $N_{OVG} = 4.95 \times 10^{14}$, we estimate $N_{ICG-OVG} \approx 8$ for OVGs fabricated at $\phi = 200$. For OVGs fabricated at $\phi = 10$, we estimate $N_{ICG-OVG}$ as ≈ 157 based on $N_{OVG} = 2.46 \times 10^{13}$.

2.5.5 Immunohistochemical staining of OVGs

Immunohistochemical staining assay was used to further validate the successful conjugation of OVGs with anti-HER2. Functionalized OVGs were targeted in OVG

suspension buffer using goat-anti-rabbit alkaline phosphatase (AP) conjugated secondary antibody. OVG suspension buffer, non-functionalized OVGs, and anti-HER2-functionalized OVGs were incubated with a goat anti-rabbit alkaline-phosphatase secondary antibody for 2 hours (Figure S3). After incubation, solutions were centrifuged at $\approx 153,000 \times g$ relative centrifugal force (RCF) for 45 minutes to remove unbound secondary antibody. The washing step was repeated three times, and the pellets were re-suspended in OVG suspension buffer. Free alkaline phosphatase conjugated antibody was prepared at similar concentration to that used during the incubation period. All samples were subsequently incubated with the alkaline phosphatase substrate 5-Bromo- 4-Chloro-3-Indolyl Phosphate (BCIP) for 30 minutes at room temperature, at this point Nitroblue Tetrazolium (NBT) was added and the samples were immediately. The alkaline phosphatase assay is a colorimetric assay in which a change to a dark-purple indicates enzymatic activity, and thus, the presence of the secondary/primary antibodies. The intensity of the images corresponding to functionalized OVGs and the positive control (Free AP conjugated antibody) (obtained after adding false color and processing using ImageJ) are nearly identical. Suspension buffer and non-functionalized OVGs show little to no color change, indicating that there was no undesired pelleting of unbound antibodies, and confirming successful conjugation of anti-HER2 monoclonal antibody to the surface of the OVGs.

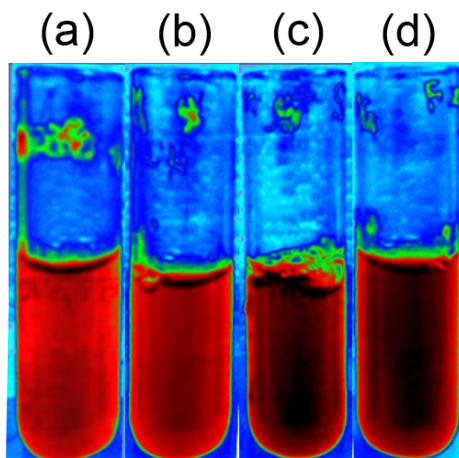


Figure 11 Immunohistochemical staining of functionalized-OVG with goat-anti-rabbit alkaline phosphatase conjugated secondary antibody. Color change indicated alkaline phosphatase activity. Samples include (a) suspension buffer, (b) non-functionalized OVGs, (c) free alkaline-phosphatase conjugated antibody and (d) anti-HER2-functionalized OVGs. The ϕ value used to fabricate both non-functionalized and functionalized OVGs was 10. Both types of OVGs were fabricated using a single fabrication method.

2.5.6 Flow cytometry results

The number of OVCAR3 and SKOV3 cells exhibiting ICG fluorescence signal, in response to incubation to various reagents are provided in Figure S4. Data shown in Figures S4(a) and S4(b) were used to generate the results presented in Figure 6a. Results presented in Figure 6b were generated using the data shown in Figure S4(c). The ϕ value used to fabricate both non-functionalized and functionalized OVGs was 10.

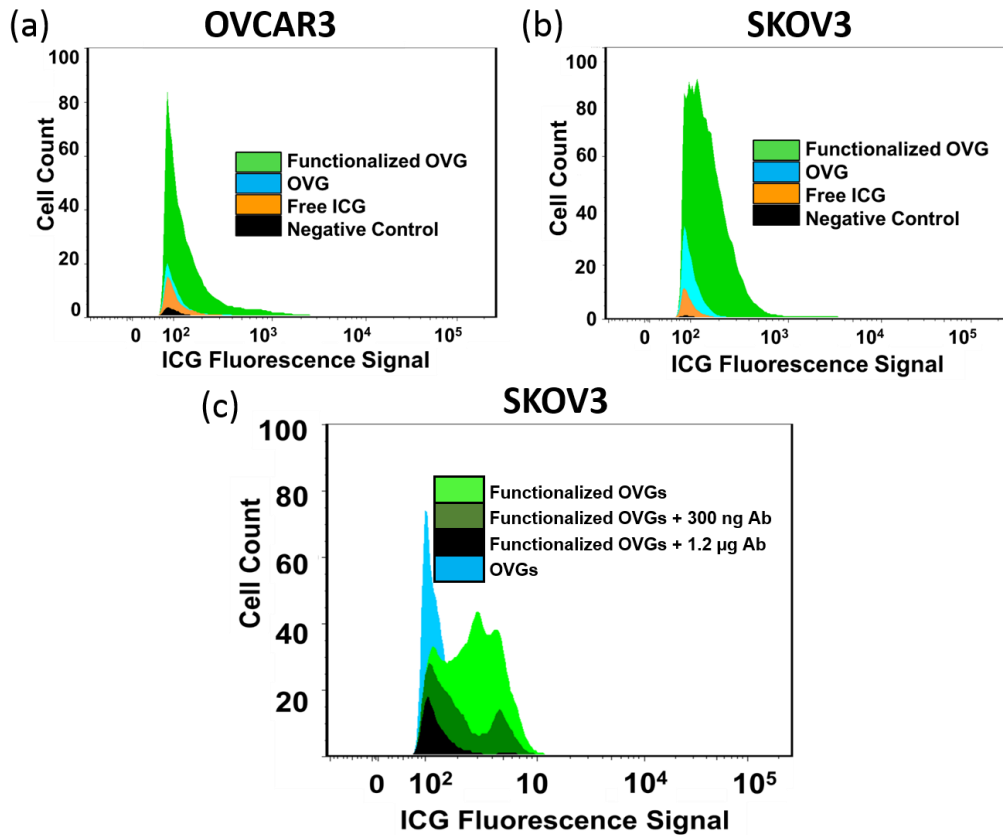


Figure 12 The number of OVCAR3 and SKOV3 cell exhibiting ICG fluorescent signals as determined by flow cytometry. We present the results for OVCAR3 (a) and SKOV3 (b) cells after 45 minutes of incubation at 4 °C with OVG suspension buffer (negative control), ICG (positive control), OVGs, and anti-HER2-functionalized OVGs. In panel (c), SKOV3 cells were incubated with ICG, OVGs, functionalized OVGs, and anti-HER2f-functionalized OVGs for 2 hours at 37 °C. Incubation with the functionalized OVGs was performed in the absence, or presence of 300 ng or 1.2 μg of anti-HER2 antibody.

CHAPTER 3: Virus-Mimicking Nano-Constructs as Platforms for NIR Fluorescence Imaging of Stage I- Sized Ovarian Cancer Tumors

3.1 INTRODUCTION

In recent years, the application of nano-sized constructs for the diagnosis and treatment of disease has grown exponentially with considerable focus being placed on their potential healthcare impacts in oncology. Of particular interest are optically active nanoconstructs used as NIR fluorescence imaging agents as they rely on NIR light (~650-1450nm). Longer wavelengths are especially advantageous due to low absorbance and autofluorescence of biological tissues resulting in increased light penetration, sensitivity and increased signal to noise ratio due as a result of decreased background interference.^{5,}

6, 77

A diverse set of materials have been explored for the encapsulation of organic NIR dyes ranging from synthetic polymers^{21, 22, 66, 78}, micelles⁷⁹⁻⁸¹, liposomes⁸² and more recently biological derivatives^{23, 26, 83, 84}. Each material may have properties that warrants its use, nonetheless there has been a recent shift to biologically derived nanoconstructs due to their innate properties. Viral protein based materials, specifically those derived from plant viruses, provide a highly versatile platform that can self-assemble into highly monodisperse, biocompatible constructs, and be chemically modified through green chemistry methods by making use of surface accessible residues.⁸⁴⁻⁸⁹

We make use of genome-depleted brome mosaic virus (BMV) to isolate individual capsid proteins (CP) and subsequently reassemble them encapsulating ICG at concentrations available in solution²⁴⁻²⁶. We refer to these constructs as optical viral ghosts (OVGs) as only a barren shell is used to encapsulate ICG.

ICG ($C_{43}H_{47}N_2NaO_6S_2$; molecular weight ~ 775 Da) is of particular importance due to its broad range of applications and sustained use since the late 1950's⁷, it remains the only NIR dye approved by the FDA for cardiovascular measurements, liver function tests and ophthalmological imaging.^{8, 9} ICG is currently being investigated for use outside of its established clinical applications for early cancer detection and aide in surgical procedures¹⁰.

Early cancer detection is indispensable for successful treatment and reduced disease recurrence rates. In the case of ovarian cancer only 20% of cases are diagnosed before metastasis at stage I (1-5mm diameter) and have limited survival (20%) when diagnosed at higher stages (II-IV),^{2, 3} leading to an estimated 14,180 deaths in 2015 alone¹. Treatment of ovarian cancer is a two-pronged approach with cytoreductive surgery being the primary method of treatment followed by chemotherapy^{33, 34}. The degree of success in cytoreductive surgery is an important prognostic factor, with improved survival associated with complete resection of all visible cancer^{35, 36}. Ideally, NIR fluorescence imaging would prove useful in both early detection of disease and as a surgical aid allowing for the visualization of small tumor deposits (<1 mm) undetectable with current technologies.

For cancer biology applications ideal organic NIR dyes should have high molar absorption coefficients and quantum yield, be chemically stable and photostable under biological conditions and possess good hydrophilicity to reduce dye aggregation.^{11, 12} ICG encapsulation helps to eliminate some of the dye's disadvantages including aqueous instability, chemical and photo-degradation, self-aggregation and high protein binding.¹⁵⁻¹⁹ ICG's relative emission levels compared to other organic NIR dyes are still low despite encapsulation and issues of dye aggregation are actually further amplified in a reduced nano-environment.

In an attempt to more efficiently image small cancer nodules in a small animal model we make use of BrCy-106 ($C_{36}H_{42}Br_2N_2O_3S_3$; molecular weight ~ 935 Da), a new organic NIR dye from Nanoquantum Sciences. Its spectral properties include absorption and emission maximum at 745 and 775nm respectively in phosphate buffer and a quantum yield 4-5 times higher than ICG (16%). Furthermore, BrCy-106 does not suffer from chemical stability issues in aqueous buffer and most importantly its tendency to self-aggregate is considerably lower.

We report the first use of ICG and BrCy-106 as contrast agents for the detection of small tumor nodules (<5 mm) in a small animal model in their free form as well as encapsulated in our virus-like nano-constructs. We detail the optical properties of our optical viral ghosts (OVGs) when encapsulating ICG or BrCy-106 and proceed to the optimization of our nanoconstructs based on ϕ -value.

3.2 METHODS

3.2.1 Reagents

Indocyanine green (Sigma Aldrich, St. Louis, MO) and BrCy-106 (Nanoquantum Sciences, Bellevue, WA) were dissolved in high purity deionized water at two concentrations; 645 μM or 64.5 μM and stored at $-20\text{ }^{\circ}\text{C}$. Methoxy-poly(ethylene glycol)-butyraldehyde (PEG-ALD, MW=5,000 Da) and butyraldehyde-PEG-butyrinaldehyde (ALD-PEG-ALD, MW= 10,000 Da) (Laysan Bio Inc., Arab, AL) were stored at $-20\text{ }^{\circ}\text{C}$ in the absence of oxygen. The reducing agent, sodium dithionite ($\text{Na}_2\text{S}_2\text{O}_4$) (Sigma Aldrich, St. Louis, MO) was suspended to 20 mM an hour prior to its use. Mouse monoclonal antibody (9G6): sc-08 against HER2 (Santa Cruz Biotechnology, Dallas, TX) at a concentration of 100 $\mu\text{g}/\text{ml}$ was stored at $4\text{ }^{\circ}\text{C}$ and used as received.

3.2.2 OVG Fabrication

Viral constructs were prepared as previously reported.²⁴⁻²⁶ After fabrication we collected the solution from the dialysis membrane, centrifuged at $\approx 262,000 \times g$ RCF for one hour to pellet dye-containing virions, and removed the supernatant. BMV suspension buffer (0.05 M NaAc, 0.008 M MgAc, pH=4) equivalent in volume to the original fabrication volume was added to the pellet, and the solution was stored overnight at $4\text{ }^{\circ}\text{C}$. BMV suspension buffer was used when determining the optical properties of dye-loaded OVGs. For particles to be used *in-vivo*, an ultra-centrifugal filter unit (Millipore, Billerica, MA) with molecular weight cut-off (MWCO) of 100 kDa was used to gently wash the particles and replace the diluent with RNA assembly buffer(50 mM Tris-HCl, 50 mM NaCl, 10 mM KCl, 5 mM MgCl₂, and 1 mM DTT, pH7.2).

As previously reported we define ϕ as the ratio of BMV CP concentration (mg/ml) to that of dye ($\mu\text{g/ml}$) used during the OVG fabrication process. When studying loading dynamics of OVGs we held dye constant at $5 \mu\text{g/ml}$ and adjusted capsid protein between 20mg/ml and 5000mg/ml to obtain the respective ϕ -range of 4-1000. For the complementary study we held capsid protein constant at 1mg/ml and adjusted dye concentrations between $100 \mu\text{g/ml}$ and $1 \mu\text{g/ml}$ to obtain a similar ϕ -range of 10-1000. When comparing optical properties of both encapsulated dyes excitation was applied at 720nm and emission was collected from 735nm - 900nm .

3.2.3 Spectroscopy

The hydrodynamic diameters of OVGs and functionalized OVGs were measured by DLS. Absorption spectra in the range of $260\text{-}900 \text{ nm}$ were obtained using a UV-VIS-NIR spectrophotometer (Cary 50, Varian Inc., Santa Clara, CA) with optical pathlength of 1 cm . NIR fluorescence spectra in response to photo-excitation at 720 nm with 450W xenon lamp were recorded in the $735\text{-}900 \text{ nm}$ spectral range using a fluorescence spectrophotometer (Fluorolog-3, Horiba –Jobin-Yvon, Inc.). Excitation-emission maps were created using the above mentioning fluorescence spectrophotometer by surveying excitation from $600\text{-}800\text{nm}$ and emission from 650nm - 900 at intervals of two nanometers.

3.2.4 Animal Protocol

Female nu/nu immunodeficient mice were purchased from Charles River Laboratories and implanted with one million cells directly into the peritoneal cavity. We used the

SKOV-3 (ATCC[®], Manassas, VA) human ovarian cancer cell line, which has relatively high expression levels of the HER2 receptor.⁹⁰ Tumors were allowed to grow to between 0.3- 0.5cm, the size was monitored using ultrasound. We carried out the animal experiment three weeks after xenografts were implanted. Five groups consisting of five animals each were formed with the following samples being injected; 1) RNA assembly buffer, 2) ICG at ~80µg/ml, 3) OVGs doped with ICG at 65 µg/ml, 4) BrCy-106 at 80µg/ml and 5) OVGs doped with BrCy-106 at 50µg/m. The difference in concentrations is due to dilution during the fabrication process. Incubation of mice after receiving 150µl of intravenously injected sample was two hours. Imaging was broken up into two days with day one containing two mice per group and day two imaging the remaining three animals per group.

3.2.5 Organ Analysis

A select subset of mice per group were imaged live at 2 hours post injection, after euthanizing the animals using compressed CO₂ gas the same subset was imaged in an open abdomen orientation. All imaging was done using an IVIS Lumina II (Caliper Life Sciences, Hopkinton, MA) set-up and images were analyzed using the available software from caliper life sciences. After euthanization the selected organs were collected; the liver, lung, stomach, small intestine, lungs, heart, kidneys spleen and tumors. Each corresponding organ was labelled and arranged with its counterpart, they were then subsequently imaged together with IVIS. The organs were flash frozen in liquid nitrogen after imaging and stored at -80°C.

To process the tumors we first incubated each organ in an individual 15ml conical tube with one milliliter of 5% SDS (weight by volume) for 30 minutes. The tumors were then homogenized using the OMNI Tissue homogenizer (OMNI International, Kennesaw, GA) by pulsing at max speed for 10-15 seconds. After thorough homogenization an additional two milliliters of 5% SDS were added and allowed to incubate for 30 minutes. After incubation the tumors were centrifuged at 12,000*g (9,000 RPM) for one hour at 10°C and one milliliter of clear supernatant was collected. Fluorescence emission spectra was collected from (735-900nm) after excitation at 720nm eliminating most tissue autofluorescence. The spectra for each group was averaged and integrated with results shown in **Figure 20**.

Organ image analysis using the IVIS II imaging software was done on all organs. Two regions of interest were made for each organ, the first a fixed size circular ROI which encompassed the organ and a portion of the surrounding background. We normalized this ROI by making an equally sized ROI of the background and subtracting it from organ ROI to eliminate any signal attributed to background. The second ROI was fitted and involved tracing the outline of the organ. Both ROI types provided us with identical trends therefore we decided to only report on fitted ROIs. ROI analysis provided us with the total emission intensity as well as the mean integrated emission (total emission intensity divided per pixel) for each organ.

3.3 Results and Discussion

3.3.1 Dye Characterization

We determined the excitation wavelengths resulting in the highest integrated emission for ICG and BrCy-106 (Figure 13) in water. BrCy-106 maximal excitation centered at 720nm with corresponding maximal emission at 775nm (Figure 13a). A reference excitation-emission map using ICG (Figure 13b) was created to reaffirm our previous knowledge of ICG, as expected the two peak excitation wavelengths were found to be 680nm and 740nm for the dimeric and monomeric forms of ICG respectively. Both of the excitation-emission maps were created at a concentration of 7 μ g/ml, the ideal concentration for maximum ICG emission. A measurement artifact results in increasing emission intensity which cannot be distinguished from the analyte's fluorescence as the surveying excitation wavelength begins to approach 800nm, specifically $\lambda > 740$ nm and $\lambda > 760$ nm for BrCy-106 and ICG. Light measured is due to Rayleigh scattering from the dissolved dye,⁹¹ which can be attenuated but not eliminated by decreasing dye concentration.

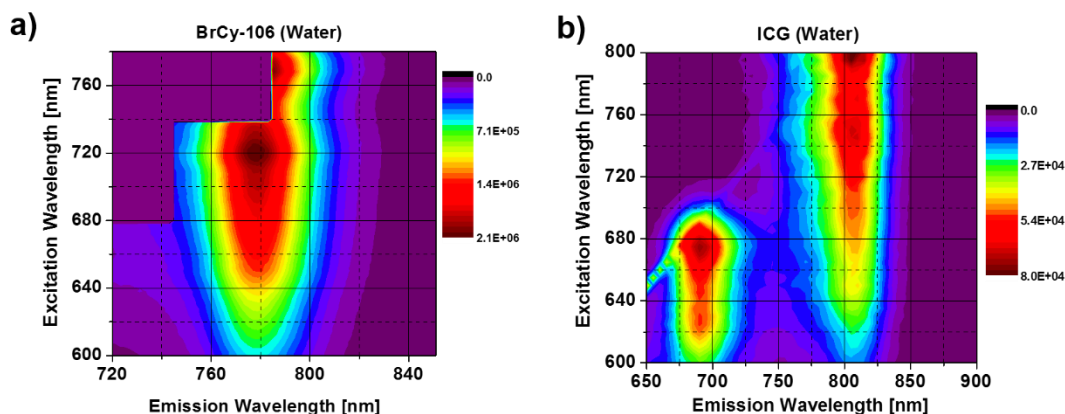


Figure 13 Excitation emission map for (a) BrCY-106 and (b) ICG in water. Both dyes were excited from 600-800nm but excitation was collected from 720-850nm and 650-900nm for BrCY-106 and ICG respectively.

The absorbance properties of BrCy-106 suspended in water, OVG suspension buffer/SAMA buffer (0.05 M NaAc, 0.008 M MgAc, pH4), RNA assembly buffer/TNKM buffer (50 mM Tris-HCl mM, 50NaCl, 10 mM KCl, 5 mM MgCl₂, and 1 mM DTT, pH7.2) and PBS were measured with the spectra of BrCy-106 in water and OVG suspension buffer shown in Figure 14. A fit of BrCy-106 peak absorbance at 745nm with increasing dye concentration showed little difference in peak absorbance when using water or OVG suspension buffer (Figure 14a). Previously published data showing optical characterization of OVGs was carried out in OVG suspension buffer^{24, 26} and considering there was little difference between the optical spectra of BrCy-106 in water or OVG suspension buffer the remaining work was carried out in OVG suspension buffer. Peak absorbance for BrCy-106 at 745nm and ICG at 780nm as a function of increasing dye concentration is shown in Figure 14b. Absorbance spectra of the dyes (Figure 14c-d) shows negligible aggregation within the range of 1-10 μ g/ml for BrCy-106 whereas ICG begins to show a strong absorbance at ~710nm indicating the formation of aggregates⁹². Decreased dye aggregation at higher concentrations is key when considering the limited volume within an OVG. Delivery of a highly concentrated payload with optimal emission properties will provide the best signal to noise ratio *in vivo*.

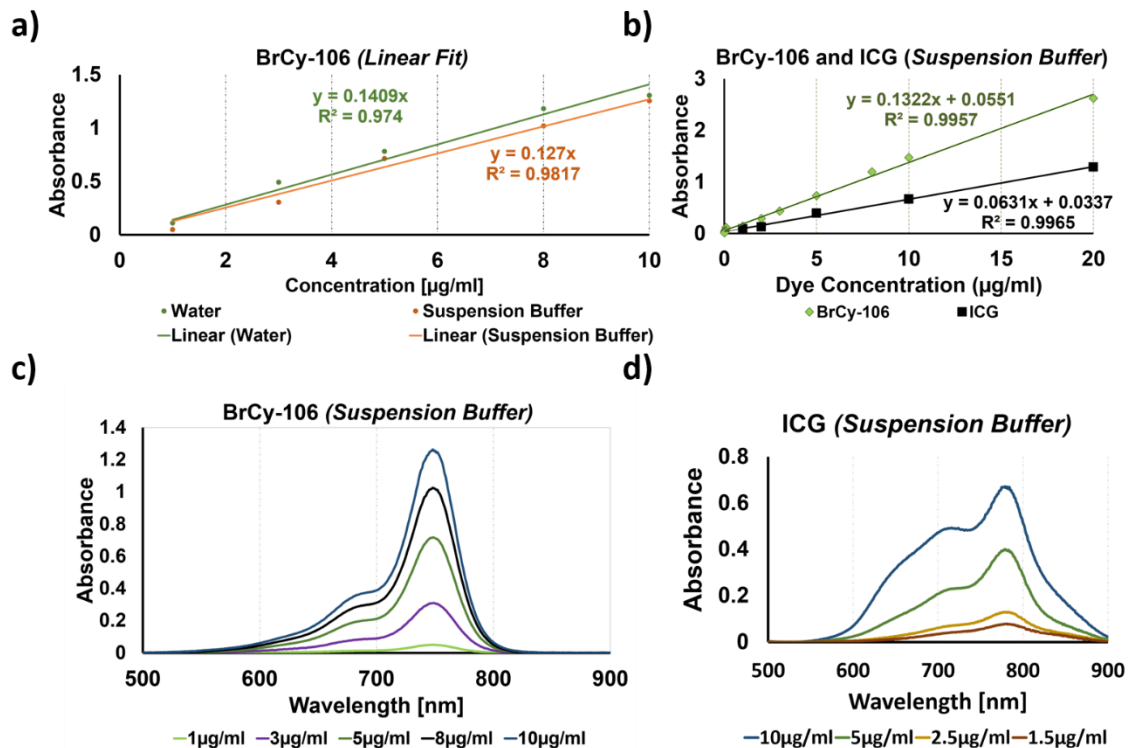


Figure 14 (a) Linear fit for peak absorbance of BrCy-106 (745nm) with water and OVG Suspension buffer as diluents. (b) Comparison of peak absorbance for BrCY-106 and ICG in OVG Suspension Buffer at 745nm and 780nm respectively. Absorbance spectra for variable dilutions of (c) BrCy-106 and (d) ICG in OVG Suspension Buffer.

With a molar extinction coefficient of $265,500 \text{ M}^{-1} \cdot \text{cm}^{-1}$ much greater than that of ICG ($24,200 \text{ M}^{-1} \cdot \text{cm}^{-1}$),⁹³ and reduced tendency to aggregate BrCy-106's has the potential for greater contrast at higher dye concentrations. Peak emission intensity was plotted against increasing concentration for BrCy-106 (at 780nm) and ICG (at 775nm past concentrations where ICG no longer emits due to dye self-aggregation. BrCy-106 continued to have emission levels higher than the ICG max peak emission at concentrations close to $50 \mu\text{g/ml}$ (Figure 15), allowing us to encapsulate nearly ten times more BrCy-106 and still create a construct with superior emission properties. At optimal

ICG concentrations (5-7 $\mu\text{g/ml}$), the integrated emission of BrCy-106 when both dyes are excited with 720nm light is ~ 20 times greater than ICG. At the maximum integrated emission for BrCy-106, the ratio between the two dyes increases to ~ 30 times. This is best rationalized by the difference in quantum yield of the two dyes, with ICG's quantum yield varying between 0.3% and 1.2% based on the diluent and BrCy-106's reported yield of 16-18% under similar conditions. Although BrCy-106 still has a ways to go in comparison to dyes such as fluorescein with quantum yields close to 90%, in terms of other similar NIR dyes such dye IR-800 which exhibit quantum yield between 7-10% BrCy-106 is near the top, more closely resembling dyes which emit at shorter wavelengths such as IR700 with a quantum yield of $\sim 24\%$.¹⁴

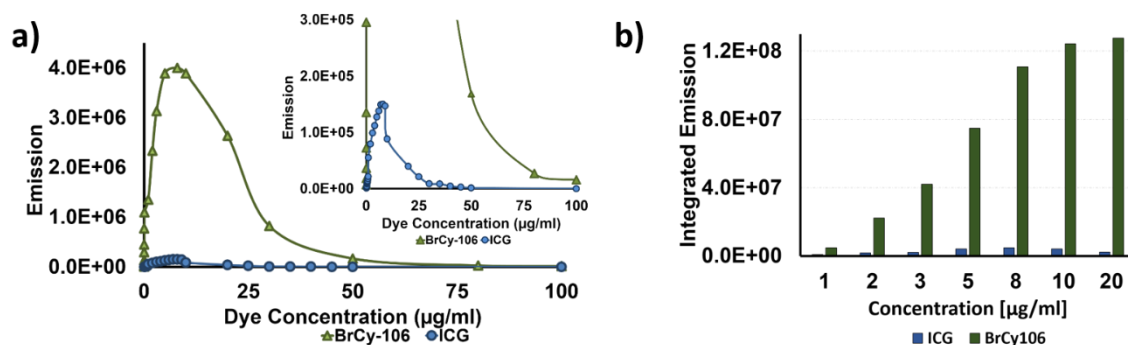


Figure 15 (a) Comparison of BrCy-106 and ICG peak emission at 775nm and 780nm after excitation at 680nm and 730nm respectively. Inset of (a) shows considerably lower ICG peak emission. (b) Integrated emission in the range of 735nm to 900nm for BrCy-106 and ICG.

Dye stability is a considerable concern especially with ICG whose fluorescence intensity tends to significantly decrease (25%) after storage at 4°C if stored for several days⁹⁴ in comparison to BrCy-106 which only slightly decreases ($< 1\%$) in the case of 3 $\mu\text{g/ml}$ (Figure 16) over a similar time period. Unlike ICG which has higher degradation

at lower concentrations BrCy-106 degrades 2.35% and 9.06% for 10 μ g/ml and 20 μ g/ml respectively. As previously shown encapsulation can further decrease dye degradation over time, even at higher temperatures (37 $^{\circ}$ C)²⁴. The trend in degradation with increase in concentration continues at -20 $^{\circ}$ C, but the decrease is considerably less with the loss in emission being only 2.88% after a year.

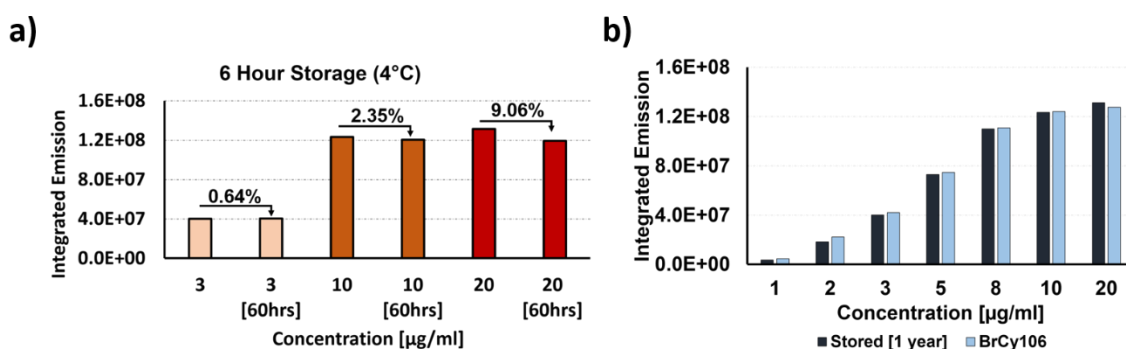


Figure 16 Integrated emission of short and long term storage of BrCy-106. Dye storage for (a) six hours at 4 $^{\circ}$ C and (b) one year at -20 $^{\circ}$ C.

3.3.2 BrCy-106 OVG Encapsulation

We have previously reported on the encapsulation of ICG with plant-infecting bromemosaic virus (BMV). ICG loading efficiency varies depending on the specific ϕ -ratio (Concentration of Capsid Protein to Concentration of Dye) used at the initial fabrication, but never falls below 90%. Our belief was that the negatively charged ICG was acting in a manner similar to native negatively charged RNA, creating a negatively charged core around which the BMV capsid protein could reform. We have subsequently been able to encapsulate a variety of dyes regardless of their charge. BrCy-106 is produced in two varieties that allow to directly conjugate antibodies or protein ligands to the dye. The first has a carboxylic functional group and has an overall positive charge while the second

formulation has an ester group and an overall negative charge. We found that both variations were able to be encapsulated with the carboxylic acid formulation having a slightly less efficient encapsulation. In an attempt to mimic our ICG encapsulating OVGs we decided to proceed only with the esterified version of BrCy-106.

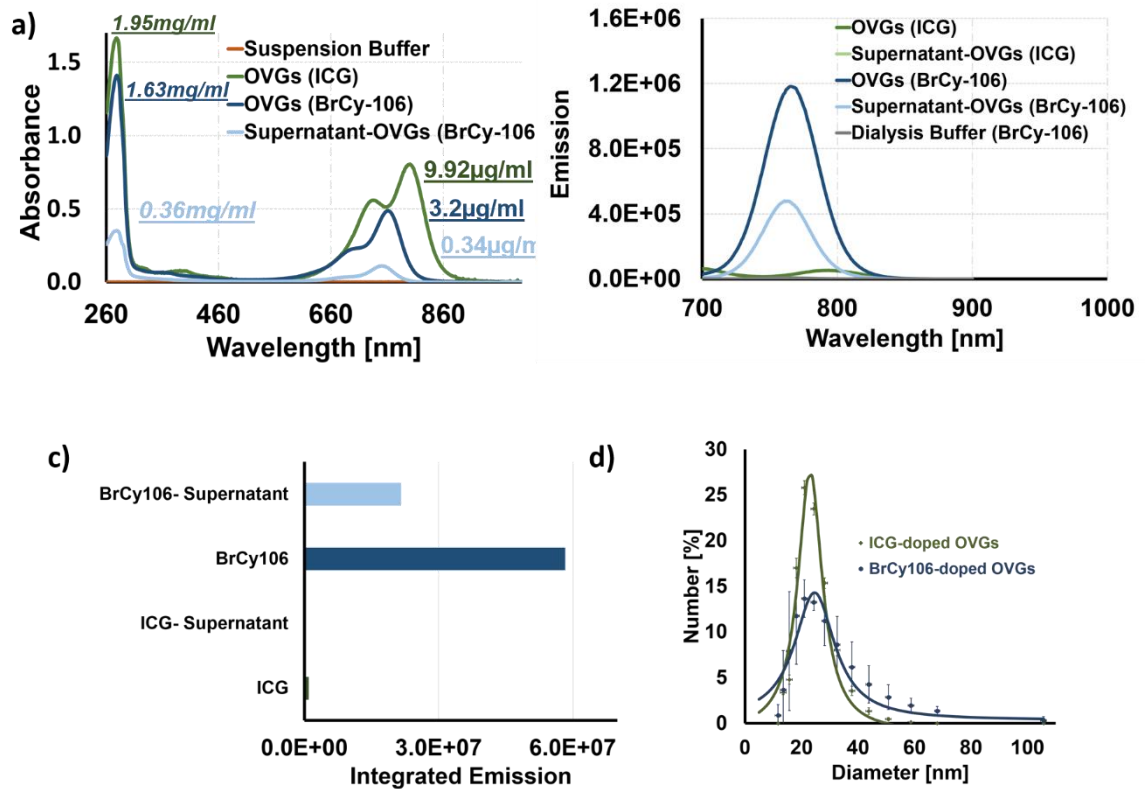


Figure 17 Comparison of encapsulation efficiency of ICG and BrCy-106 within OVGs. (a) Absorbance and (b) emission spectra of ICG encapsulating OVGs [OVGs (ICG)], BrCY-106 encapsulating OVGs [OVGs (BrCy-106)] and their corresponding supernatants after washing in response to 680nm excitation. (c) Integrated emission from 700-900nm of OVGs doped with BrCy-106 and ICG and their respective supernatants. (d) Hydrodynamic diameters of ICG and BrCY-106 doped OVGs, with n=3 measurements. OVGs were formulated at $\phi=200$ with 10μg/ml of dye and 2mg/ml of capsid protein.

OVGs were fabricated at a $\phi=200$ using BrCY-106 or ICG with 2mg/ml of BMV capsid protein and 10 μ g/ml of each respective dye with a total volume of 5ml. The fabrication volume was increased to 5ml in order to mitigate the effect of any potential losses during our centrifugation washing step. Using the absorbance calibrations from Figure 14 and the absorbance spectra of each of the dye fabrications (Figure 17a) we determined the efficiency of ICG encapsulation was 99% in this particular $\phi=200$ formulation. The efficiency of BrCy-106 was 32% with 3.4% of the initial dye remaining in the supernatant after the washing step, considering the stability of the dye at upwards of 60hrs and the fact that fabrication time was only 16hrs (Dialysis), we believe the unencapsulated dye must have excited the dialysis membrane and would be found in the dialysate at concentrations not detectable through absorbance. Despite considerably lower dye concentrations and overall lower absorbance values, BrCy-106 boasts 60 times greater integrated emission in response to 680nm excitation (Figure 17c) than ICG when constructed under identical initial conditions. We verified adequate particle fabrication by measuring the hydrodynamic diameters of the each formulation with peak values 25.4nm and 23.7nm for BrCY-106 and ICG respectively.

3.3.3 Optimizing Dye Encapsulation

We have previously tested several formulations and had decided there was a good enough trade-off between amount of dye encapsulated and fluorescence emission from OVGs fabricated at $\phi=200$ at least for *in-vivo* applications²⁶. To more precisely determine the best ϕ -value in terms of highest fluorescence emission for both dyes, we

systematically surveyed a wide range of formulations. Initially we held both dyes constant at 5 μ g/ml and varied the capsid protein concentration to achieve ϕ -values in the range of 4 and 1000 (Figure 18). This meant increasing the capsid protein concentration from 20 μ g/ml to 5000 μ g/ml. By increasing the concentration of CP we are directly increasing the total number of fabricated OVGs since there is always constant number of CPs per particle. Thus what we are essentially doing is dividing the available dye among an increasing number of particles, but we must also consider the limited amount of space within each particle and the dynamics brought about by the overcrowding of each dye within. ICG was encapsulated at over 90% efficiency at $\phi=75$ or higher, with the lowest loading efficiency of 52% at $\phi=4$ due to the physical inability to encapsulate the entirety of the dye (Figure 18b) in such few particles. The capsid protein is conserved over the ϕ -range, except for the case of $\phi=1000$ where only 82% remains most likely due to the lack of dye for proper nucleation. Capsid protein is similarly conserved in the case of BrCy-106 (Figure 18c), despite dye encapsulation efficiency being considerably lower, with $\phi=4$ at 3% and steadily increasing with ϕ -value, reaching its highest point of 52% at $\phi=1000$. Encapsulation efficiencies vary for each dye while the initial amount of capsid protein is conserved up to $\phi=500$. Integrated emission (735nm- 900nm) in response to 720nm excitation linearly increases with ϕ -value for both dyes reaching a maximum at $\phi=1000$ (Figure 18a). We compare the total integrated emission of OVGs when loaded with BrCy-106 or ICG at each ϕ -value and found the greatest difference was at lower ϕ -values where ICG suffers from decreased emission due to dye-dye aggregation.

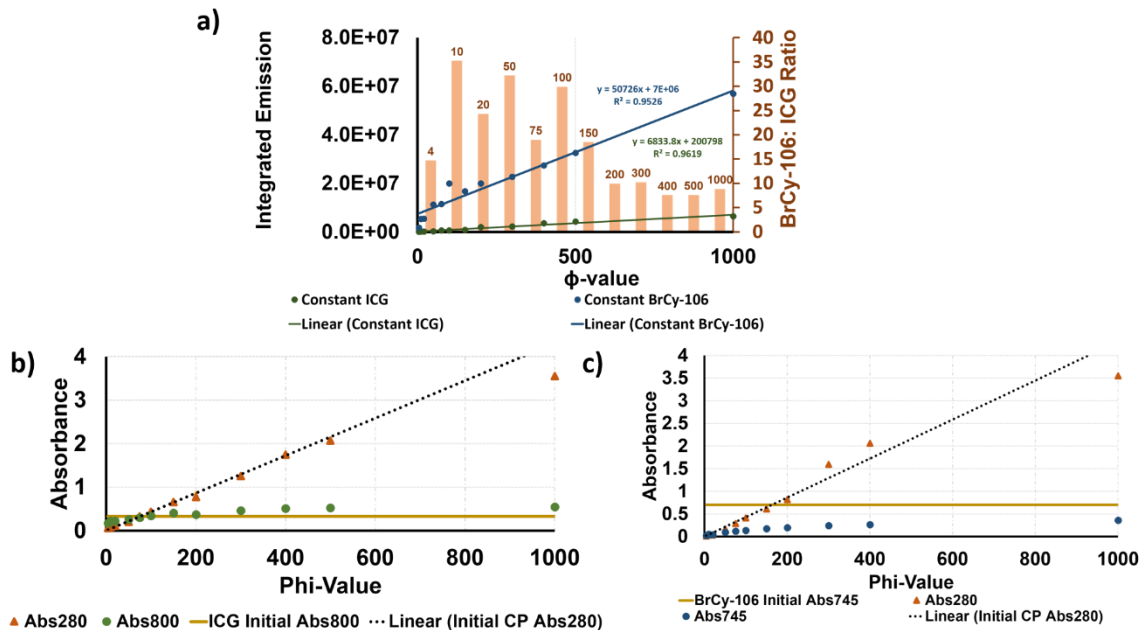


Figure 18 OVG ϕ -formulations in the 4-1000 range with dye held constant at 5 μ g/ml and varying capsid protein concentrations. (a) Integrated emission of OVGs encapsulating BrCy-106 and ICG and the respective integrated emission ratio for each surveyed ϕ -value. Characteristic peak absorbances for (b) ICG at 800nm and (c) BrCy-106 at 745nm including peak values for capsid protein at 280nm.

To further study the effect of dye-dye aggregation, we held capsid protein concentration constant at 1mg/ml and varied dye concentration between 100 μ g/ml and 1 μ g/ml to achieve a $\phi=10$ and $\phi=1000$ respectively. As seen with the data from Figure 19, ICG encapsulation efficiency remains high throughout the range, but the high concentrations of ICG lead to aggregation of particles beginning at $\phi=50$ as evident from the divergence of peak absorbance at 280nm (orange triangles) from initial fabrication capsid protein absorbance (black dotted line) (Figure 19b). Dynamic light scattering measurements (not shown) demonstrate uniform size centered at 25nm with larger agglomerates beginning to appear at $\phi=50$. Unlike ICG, when encapsulating BrCy-106

we don't see the same particle aggregation phenomena in part due to a higher threshold for dye aggregation in conjunction to a decrease in loading. The resulting trend of integrated emission with increasing ϕ -value differs between dyes. ICG loaded OVGs show a sigmoidal increase reaching their maximum and plateauing at $\phi=500$ whereas BrCy-106 loaded OVGs follow a hyperbolic behavior with a maximum at $\phi=100-200$.

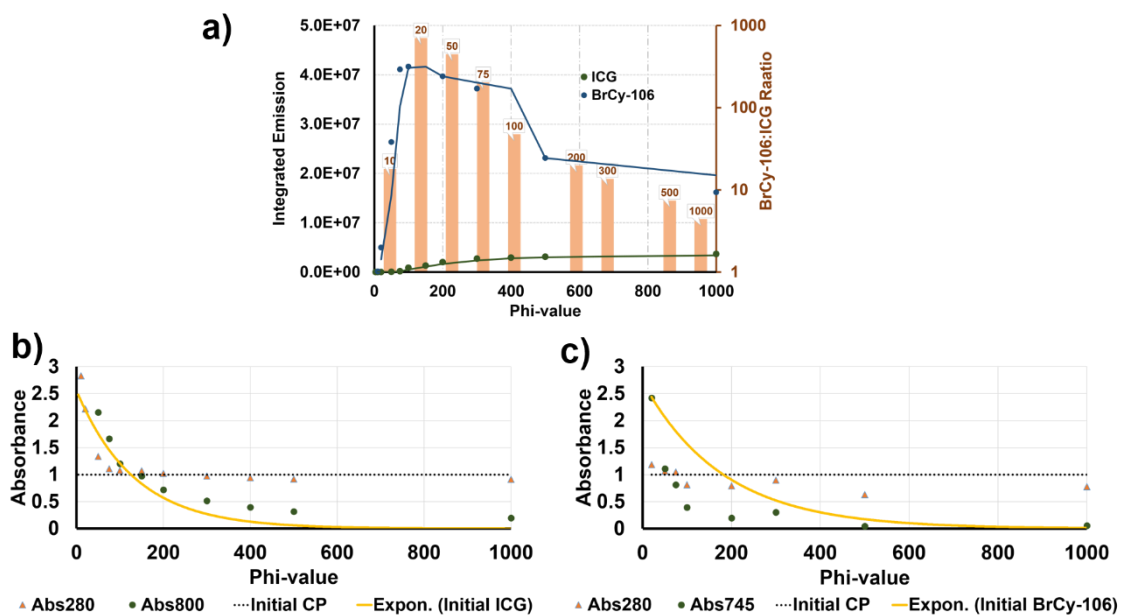


Figure 19 OVG ϕ -formulations in the 10-1000 range with capsid protein held constant at 1mg/ml and varying dye concentrations. (a) Integrated emission of OVGs encapsulating BrCy-106 and ICG and the respective integrated emission ratio for each surveyed ϕ -value. Characteristic peak absorbances for (b) ICG at 800nm and (c) BrCy-106 at 745nm including peak values for capsid protein at 280nm.

3.3.4 In-vivo Nano-construct Delivery

As previously mentioned ICG's rapid clearance from blood plasma is what drives research into alternative methods of delivery. At large concentrations 1mg/ml, ICG has successfully been used to visualize cancer nodules in mice.⁹⁵ Our group has previously

demonstrated the potential of ICG containing OVGs as vehicles for the selective visualization of high-HER2 expressing SKOV-3 ovarian cancer cell line²⁶. Xenografts of the SKOV-3 ovarian cancer cell line were implanted in female nu/nu immunodeficient mice and allowed to grow to a diameter of 0.3-0.5cm. The mice were broken down into five groups with five animals per group. The groups included RNA assembly buffer (control), ICG, BrCy-106, OVGs loaded with ICG and OVGs loaded with BrCy-106. The total concentration of each group was set in $\mu\text{g/ml}$ by using $100\mu\text{M}$ of ICG as the set point. Stocks of each dye were prepared in RNA assembly buffer to a concentration of $77\mu\text{g/ml}$ ($100\mu\text{M}$). ICG loaded OVGs were concentrated to $65\mu\text{g/ml}$ while BrCy-106 loaded OVGs were concentrated to $50\mu\text{g/ml}$ in RNA assembly buffer. OVGs were fabricated at $\phi=200$ with initial dye concentrations of $5\mu\text{g/ml}$ and initial capsid protein concentration of 1mg/ml . The OVG samples were concentrated to achieve a 15X concentration using a centrifugal filter unit. The differences in final dye concentration are due to unavoidable particle and dye loss as a result of using the centrifugal filter unit. The absorbance spectra of dye encapsulating OVGs after concentration shows that absorbance of capsid protein at 280nm in Figure 20a are identical between the two constructs indicating that any particle loss was uniform, nonetheless, there was greater dye loss from within the BrCy-106 particles. In addition there was also unequal dye loading during fabrication, with ICG always encapsulating nearly 100% of dye and roughly 50% loading in the case of BrCy-106. Instead of adding a greater number of particles to correct the difference in total dye we normalized to particle number.

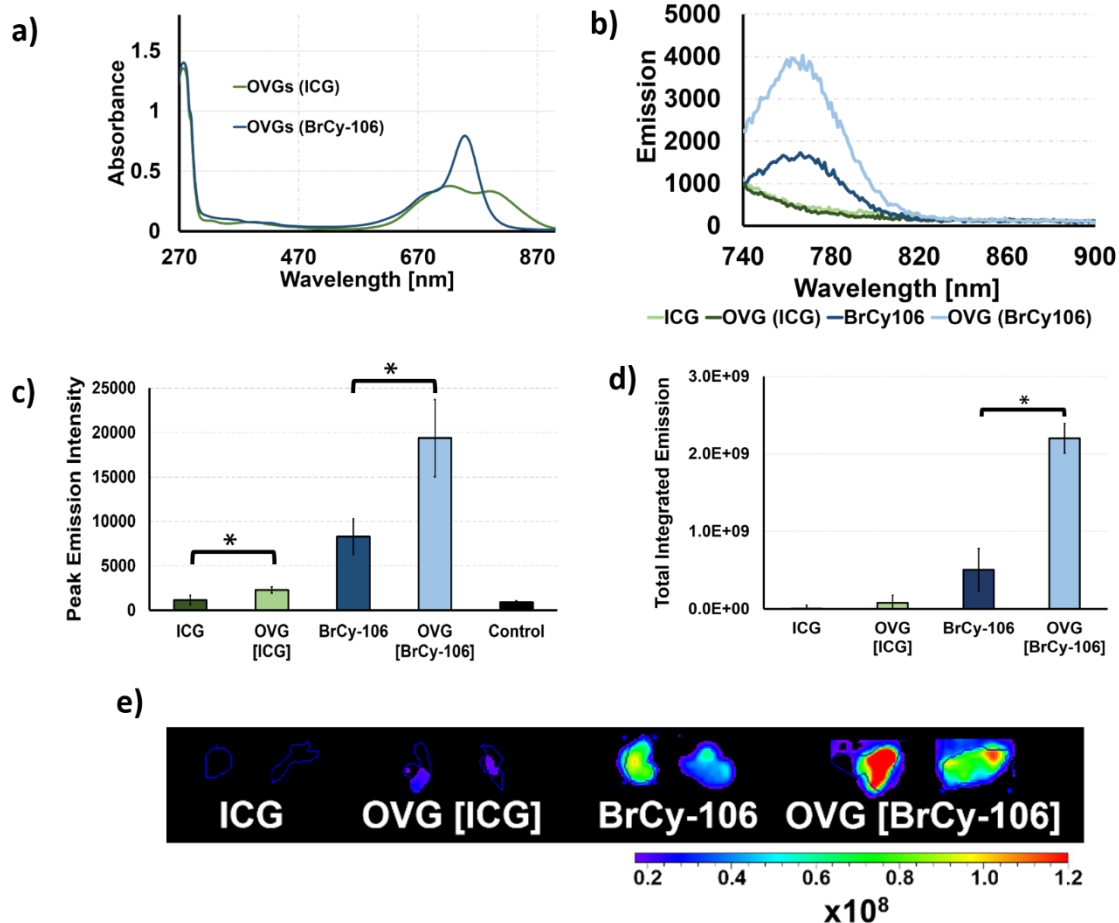


Figure 20 (a) Absorbance spectra of samples used for mice studies. All measurements are shown at a 1:10 dilution. Average emission spectra of n=5 homogenized tumors after 720nm excitation presented as (b) a spectra and (c) histogram form after weight normalization. (d) Image analysis using fitted ROIs of tumor samples on n=2 data set. Two-tailed t-test was performed on the data with $p < 0.05$ indicated by (*).

Each animal was injected with 150 μ l of its respective sample and incubated for 2 hrs. After euthanization, organ imaging and collection we homogenized all tumor samples. Figure 20b shows the resulting average spectral emission in response to 720nm excitation of all tumor samples. Mice were injected with significantly less total dye in the form of BrCy-106 doped OVGs when compared to free BrCy-106, nonetheless, tumor sample

homogenization shows a clearly higher signal from the BrCy-106 delivered in nano-construct form. We display the processed organ information once more in Figure 20c but include a correction factor to account for the differences in initial dye concentrations and normalize each of the averaged tumor samples by their weight prior to homogenization. In the case of BrCy-106 increased tumor localization is a clear result of encapsulation although this is not entirely obvious for ICG but it becomes clear after performing a two tailed t-test (Figure 20c) We believe that similar numbers of nano-constructs were localized to the tumors regardless of dye type encapsulated and that the apparent differences in emission levels are due strictly to the superior optical properties of BrCy-106. Captured images using the IVIS II system taken immediately after euthanization of the mice were processed by drawing regions of interest (ROIs) around the organ boundaries and measuring the total integrated emission within each ROI. Due to the large number of mice the experiment was broken up into two days which resulted in two imaging sessions. The difference in emission intensities between days were considerable and had to be treated separately for the purposes of the image analysis. Although the trends are identical for both days too much error would be added if the two separate imaging data sets were to be combined. The imaging data for day one is shown in Figure 20d-e. Not only is higher localization of encapsulated dye visually obvious, but we also show very close fit between homogenized organs and data extracted from *ex-vivo* imaging.

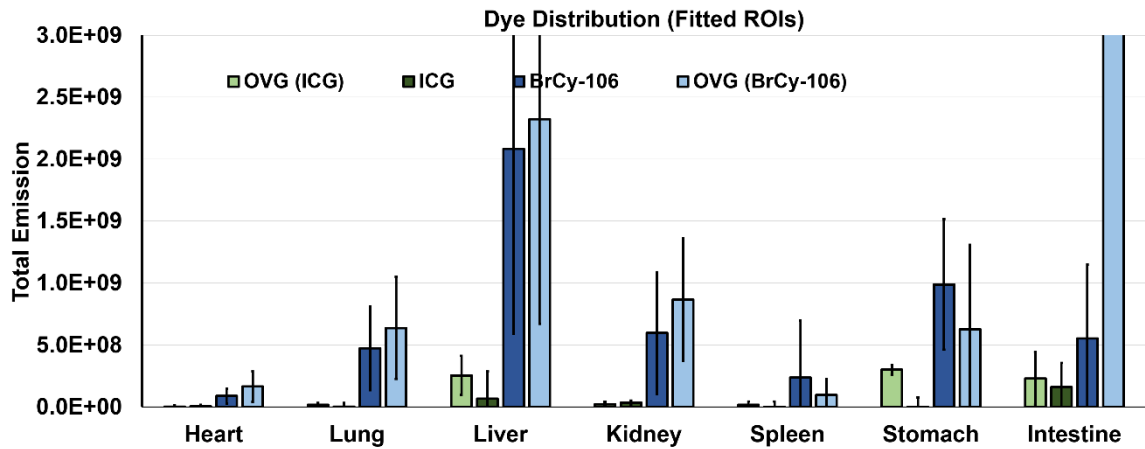


Figure 21 Histogram of dye distribution in mice. Data corresponds to image processing using fitted ROIs on n=5 data set.

Dye buildup based on dye type and delivery vehicle or lack of in organs after two hour incubation was compared through ROI image analysis (Figure 21). Except in the case of the intestine, dye clearance and buildup by the remaining organs appears to be unchanged by the encapsulation of BrCy-106 or ICG as evident by similar fluorescence intensity in the organs. There are large differences in total emission levels between BrCy-106 and ICG in either form, but we believe this to be associated with the higher emission levels of BrCy-106 rather than any differences in clearance rates.

3.4 CONCLUSIONS

To the best of our knowledge this is the first use of BMV virus-resembling nanoconstructs used for the detection of small (>5mm) cancer nodules in a small animal model. We optimize our previously reported virus-resembling nano-constructs and demonstrate for the first time their ability to encapsulate distinct dyes regardless of ionic charge or size. Subsequently we demonstrate the effectiveness of our OVG constructs to

increase the localization of dye to tumor nodules after only 2 hours. These constructs could help improve early detection and disease management by providing the capability for detection and imaging of otherwise undetectable nodules. As we have previously shown specific delivery is possible through surface functionalization by making use of surface-accessible amine-terminated residues on our viral nano-constructs²⁶. Surface functionalized OVGs doped with BrCy-106 for targeted delivery could more effectively be used for small tumor NIR fluorescence imaging increasing their efficacy in early disease detection.

CHAPTER 4: CONCLUSION

This study describes the development of a new type of near-infrared optical probe for visualization of disease, first making use of ICG and subsequently BrCy-106. In the second chapter we demonstrate successful conjugation of our OVG nanoconstructs composed of BMV doped with ICG. Using spectroscopy and dynamic light scattering along with several immunohistochemical assays we verify the successful conjugation on anti-HER2 antibody to the surface of OVGs. Through fluorescence imaging and flow cytometry we investigate the specificity of our functionalized vehicles and find a highly dose dependent response in particle uptake by SKOV3 cells. Uptake can be reduced to free ICG levels through the co-incubation of functionalized OVGs and excess competitive antibody.

We begin testing the functionality of OVGs to image SKOV3 derived ovarian cancer tumors in nu/nu mice after incubation at two, six and 24 hours. Visualization is possible but success is limited due to poor fluorescence emission. In chapter three we optimize OVGs to determine the fabrication parameters that achieve the highest fluorescence emission. Nano-constructs are doped with BrCy-106 to compare the potential of using a distinct NIR dye either in conjunction or instead of ICG. We demonstrate the effectiveness of our OVG constructs to increase the localization of dye to tumor nodules after only 2 hours.

We have shown the first use of virus-resembling nano-constructs as NIR optical probes for the specific targeting and fluorescence imaging of ovarian cancer cell lines. Using both ICG and BrCy-106 doped OVGs we demonstrate the successful imaging of

small (<5mm) SKOV3 tumors in an immunocompromised mice model. These virus-resembling nano-constructs could help improve the clinical management of ovarian cancer by providing the capability for detection and imaging of otherwise undetectable nodules when used in conjunction with open surgical procedures.

REFERENCES

1. Siegel, R. L.; Miller, K. D.; Jemal, A. Cancer statistics, 2015. *CA Cancer J. Clin.* 2015, 65, 5-29.
2. Heintz, A. P. M.; Odicino, F.; Maisonneuve, P.; Quinn, M. A.; Benedet, J. L.; Creasman, W. T.; Ngan, H. Y. S.; Pecorelli, S.; Beller, U. Carcinoma of the Ovary. *Int. J. Gynecol. Obstet.* 2006, 95, Supplement 1, S161-S192.
3. Cancer Facts & Figures 2011.
<http://www.cancer.org/Research/CancerFactsFigures/CancerFactsFigures/cancer-facts-figures-2011>.
4. Libutti, S. K.; Choyke, P.; Choy, G. Current Advances in Molecular Imaging: Noninvasive In Vivo Bioluminescent and Fluorescent Optical Imaging in Cancer Research. *Mol. Imaging* 2003, 2, 303-312.
5. Pansare, V. J.; Hejazi, S.; Faenza, W. J.; Prud'homme, R. K. Review of Long-Wavelength Optical and NIR Imaging Materials: Contrast Agents, Fluorophores, and Multifunctional Nano Carriers. *Chem. Mater.* 2012, 24, 812-827.
6. Simpson, C. R.; Kohl, M.; Essenpreis, M.; Cope, M. Near-infrared optical properties of ex vivo human skin and subcutaneous tissues measured using the Monte Carlo inversion technique. *Phys. Med. Biol.* 1998, 43, 2465-2478.
7. Fox, J. J.; Wood, E. H. Application of dilution curves recorded from the right side of the heart or venous circulation with the aid of a new indicator dye. *Proc. Mayo Clin* 1957, 32, 541.
8. Kusano, M.; Tajima, Y.; Yamazaki, K.; Kato, M.; Watanabe, M.; Miwa, M. Sentinel node mapping guided by indocyanine green fluorescence imaging: A new method for sentinel node navigation surgery in gastrointestinal cancer. *Dig. Surg.* 2008, 25, 103-108.
9. Alander, J. T.; Kaartinen, I.; Laakso, A.; Pätilä, T.; Spillmann, T.; Tuchin, V. V.; Venermo, M.; Välisuo, P. A Review of Indocyanine Green Fluorescent Imaging in Surgery. *International Journal of Biomedical Imaging* 2012, 2012, 940585.
10. Polom, K.; Murawa, D.; Rho, Y. S.; Nowaczyk, P.; Hunerbein, M.; Murawa, P. Current trends and emerging future of Indocyanine Green usage in surgery and oncology A Literature Review. *Cancer* 2011, 117, 4812-4822.
11. Luo, S.; Zhang, E.; Su, Y.; Cheng, T.; Shi, C. A review of NIR dyes in cancer targeting and imaging. *Biomaterials* 2011, 32, 7127-7138.

12. Masotti, A.; Vicennati, P.; Boschi, F.; Calderan, L.; Sbarbati, A.; Ortaggi, G. A Novel Near-Infrared Indocyanine Dye–Polyethylenimine Conjugate Allows DNA Delivery Imaging in Vivo. *Bioconjug. Chem.* 2008, 19, 983-987.
13. Philip, R.; Penzkofer, A.; Baumler, W.; Szeimies, R. M.; Abels, C. Absorption and fluorescence spectroscopic investigation of indocyanine green. *J. Photoch. Photobio. A* 1996, 96, 137-148.
14. Hong, G.; Tabakman, S. M.; Welsher, K.; Chen, Z.; Robinson, J. T.; Wang, H.; Zhang, B.; Dai, H. Near-Infrared-Fluorescence-Enhanced Molecular Imaging of Live Cells on Gold Substrates. *Angew. Chem. Int. Ed.* 2011, 50, 4644-4648.
15. Saxena, V.; Sadoqi, M.; Shao, J. Degradation kinetics of indocyanine green in aqueous solution. *J. Pharm. Sci.* 2003, 92, 2090-2097.
16. G. R. Cherrick; S. W. Stein; C. M. Leevy; Davidson, C. S. Indocyanine green: Observations on its physical properties, plasma decay, and hepatic extraction. *J. Clin. Invest.* 1960, 39, 592-600.
17. Muckle, T. J. Plasma-proteins binding of indocyanine green. *Biochem. Med.* 1976, 15, 17-21.
18. Yoneya, S.; Saito, T.; Komatsu, Y.; Koyama, I.; Takahashi, K.; Duvoll-Young, J. Binding properties of indocyanine green in human blood. *Invest. Ophthalmol. Vis. Sci.* 1998, 39, 1286-1290.
19. Desmettre, T.; Devoisselle, J. M.; Mordon, S. Fluorescence Properties and Metabolic Features of Indocyanine Green (ICG) as Related to Angiography. *Surv. Ophthalmol.* 2000, 45, 15-27.
20. Bahmani, B.; Gupta, S.; Upadhyayula, S.; Vullev, V. I.; Anvari, B. Effect of polyethylene glycol coatings on uptake of indocyanine green loaded nanocapsules by human spleen macrophages in vitro. *Journal of Biomedical Optics* 2011, 16.
21. Bahmani, B.; Lytle, C. Y.; Walker, A. M.; Gupta, S.; Vullev, V. I.; Anvari, B. Effects of nanoencapsulation and PEGylation on biodistribution of indocyanine green in healthy mice: quantitative fluorescence imaging and analysis of organs. *Int. J. Nanomed.* 2013, 8, 1609-1620.
22. Bahmani, B.; Guerrero, Y.; Bacon, D.; Kundra, V.; Vullev, V. I.; Anvari, B. Functionalized polymeric nanoparticles loaded with indocyanine green as theranostic materials for targeted molecular near infrared fluorescence imaging and photothermal destruction of ovarian cancer cells. *Lasers Surg. Med.* 2014, 46, 582-592.

23. Bahmani, B.; Bacon, D.; Anvari, B. Erythrocyte-derived photo-theranostic agents: hybrid nano-vesicles containing indocyanine green for near infrared imaging and therapeutic applications. *Sci. Rep.* 2013, 3, 2180.
24. Jung, B.; Rao, A. L. N.; Anvari, B. Optical nano-constructs composed of genome-depleted brome mosaic virus doped with a near infrared chromophore for potential biomedical applications. *ACS Nano* 2011, 5, 1243-1252.
25. Jung, B.; Anvari, B. Virus-mimicking optical nanomaterials: near infrared absorption and fluorescence characteristics and physical stability in biological environments. *ACS Appl. Mater. Inter* 2013, 5, 7492-7500.
26. Guerrero, Y. A.; Bahmani, B.; Singh, S., P.; Vullev, V., I.; Kundra, V.; Anvari, B. Virus-resembling nano-structures for near infrared fluorescence imaging of ovarian cancer HER2 receptors. *Nanotechnology* 2015, 26, 435102.
27. Steinmetz, N. F.; Manchester, M. PEGylated viral nanoparticles for biomedicine: The impact of PEG chain length on VNP cell interactions in vitro and ex vivo. *Biomacromolecules* 2009, 10, 784-92.
28. Kaiser, C. R.; Flenniken, M. L.; Gillitzer, E.; Harmsen, A. L.; Harmsen, A. G.; Jutila, M. A.; Douglas, T.; Young, M. J. Biodistribution studies of protein cage nanoparticles demonstrate broad tissue distribution and rapid clearance in vivo. *Int. J. Nanomed.* 2007, 2, 715-733.
29. Singh, P.; Prasuhn, D.; Yeh, R. M.; Destito, G.; Rae, C. S.; Osborn, K.; Finn, M. G.; Manchester, M. Bio-distribution, toxicity and pathology of cowpea mosaic virus nanoparticles in vivo. *J. Control. Release* 2007, 120, 41-50.
30. Yildiz, I.; Shukla, S.; Steinmetz, N. F. Applications of viral nanoparticles in medicine. *Curr. Opin. Biotechnol.* 2011, 22, 901-908.
31. Cancer Facts & Figures 2014.
<http://www.cancer.org/acs/groups/content/@research/documents/webcontent/acspc-042151.pdf>.
32. Heintz, A. P. M.; Odicino, F.; Maisonneuve, P.; Quinn, M. A.; Benedet, J. L.; Creasman, W. T.; Ngan, H. Y. S.; Pecorelli, S.; Beller, U. Carcinoma of the Ovary. *Int. J. Gynecol. Obstet* 2006, 95, Supplement 1, S161-S192.
33. Hoskins, W. J. Surgical staging and cytoreductive surgery of epithelial ovarian-cancer. *Cancer* 1993, 71, 1534-1540.
34. Ozols, R. F. Ovarian-Cancer. 2. Treatment. *Curr. Probl. Cancer* 1992, 16, 63-126.

35. Zivanovic, O.; Aldini, A.; Carlson, J. W.; Chi, D. S. Advanced cytoreductive surgery: american perspective. *Gynecol. Oncol.* 2009, 114, S3-S9.
36. Vergote, I.; van Gorp, T.; Amant, F.; Leunen, K.; Neven, P.; Berteloot, P. Timing of debulking surgery in advanced ovarian cancer. *Int. J. Gynecol. Cancer* 2008, 18, 11-19.
37. Loo, C.; Lowery, A.; Halas, N. J.; West, J.; Drezek, R. Immunotargeted nanoshells for integrated cancer imaging and therapy. *Nano Lett.* 2005, 5, 709-711.
38. Escobedo, J. O.; Rusin, O.; Lim, S.; Strongin, R. M. NIR dyes for bioimaging applications. *Curr. Opin. Chem. Biol.* 2010, 14, 64-70.
39. Lanitis, E.; Dangaj, D.; Hagemann, I. S.; Song, D. G.; Best, A.; Sandaltzopoulos, R.; Coukos, G.; Powell, D. J. Primary human ovarian epithelial cancer cells broadly express HER2 at immunologically-detectable levels. *PLoS One* 2012, 7, e49829.
40. Crane, L. M. A.; van Oosten, M.; Pleijhuis, R. G.; Motekallemi, A.; Dowdy, S. C.; Cliby, W. A.; van der Zee, A. G. J.; van Dam, G. M. Intraoperative imaging in ovarian cancer: fact or fiction? *Mol. Imaging* 2011, 10, 248-257.
41. Verri, E.; Guglielmini, P.; Puntoni, M.; Perdelli, L.; Papadia, A.; Lorenzi, P.; Rubagotti, A.; Ragni, N.; Boccardo, F. HER2/neu oncoprotein overexpression in epithelial ovarian cancer: Evaluation of its prevalence and prognostic significance - Clinical study. *Oncology* 2005, 68, 154-161.
42. Pils, D.; Pinter, A.; Reibenwein, J.; Alfanz, A.; Horak, P.; Schmid, B. C.; Hefler, L.; Horvat, R.; Reinthaller, A.; Zeillinger, R.; Krainer, M. In ovarian cancer the prognostic influence of HER2/neu is not dependent on the CXCR4/SDF-1 signalling pathway. *Br. J. Cancer* 2007, 96, 485-491.
43. Lavelle, L.; Michel, J. P.; Gingery, M. The disassembly, reassembly and stability of CCMV protein capsids. *J. Virol. Methods* 2007, 146, 311-316.
44. Meador, L. R.; Mor, T. S. Meeting Report VLPNPV: Session 5: Plant based technology. *Hum. Vaccin. Immunother.* 2014, 10, 3068-3073.
45. Huang, X. L.; Stein, B. D.; Cheng, H.; Malyutin, A.; Tsvetkova, I. B.; Baxter, D. V.; Remmes, N. B.; Verchot, J.; Kao, C.; Bronstein, L. M.; Dragnea, B. Magnetic virus-like nanoparticles in *N. benthamiana* plants: A new paradigm for environmental and agronomic biotechnological research. *Acs Nano* 2011, 5, 4037-4045.
46. Dixit, S. K.; Goicochea, N. L.; Daniel, M.-C.; Murali, A.; Bronstein, L.; De, M.; Stein, B.; Rotello, V. M.; Kao, C. C.; Dragnea, B. Quantum dot encapsulation in viral capsids. *Nano Lett.* 2006, 6, 1993-1999.

47. Liepold, L.; Anderson, S.; Willits, D.; Oltrogge, L.; Frank, J. A.; Douglas, T.; Young, M. Viral capsids as MRI contrast agents. *Magn. Reson. Med.* 2007, 58, 871-879.
48. Tsvetkova, B.; Dragnea, B. G. Encapsulation of nanoparticles in virus protein shells. *Methods Mol. Biol.* 2015, 1252, 1-15.
49. Michel, J. P.; Gingery, M.; Lavelle, L. Efficient purification of bromoviruses by ultrafiltration. *J. Virol. Methods* 2004, 122, 195-198.
50. Porterfield, J. Z.; Zlotnick, A. A simple and general method for determining the protein and nucleic acid content of viruses by UV absorbance. *Virology* 2010, 407, 281-288.
51. Annamalai, P.; Rao, A. L. N. Replication-independent expression of genome components and capsid protein of brome mosaic virus in planta: A functional role for viral replicase in RNA packaging. *Virology* 2005, 338, 96-111.
52. Annamalai, P.; Rao, A. L. N. RNA Encapsulation Assay. In *Plant Virology Protocols*, Foster, G.; Johansen, I. E.; Hong, Y.; Nagy, P., Eds. Humana Press: Totowa, New Jersey, 2008; Vol. 451, pp 251-264.
53. Tolmachev, V.; Wallberg, H.; Sandstrom, M.; Hansson, M.; Wennborg, A.; Orlova, A. Optimal specific radioactivity of anti-HER2 Affibody molecules enables discrimination between xenografts with high and low HER2 expression levels. *Eur. J. Nucl. Med. Mol. Imaging* 2011, 38, 531-539.
54. Delord, J. P.; Allal, C.; Canal, M.; Mery, E.; Rochaix, P.; Hennebelle, I.; Pradines, A.; Chatelut, E.; Bugat, R.; Guichard, S.; Canal, P. Selective inhibition of HER2 inhibits AKT signal transduction and prolongs disease-free survival in a micrometastasis model of ovarian carcinoma. *Ann. Oncol.* 2005, 16, 1889-97.
55. Jung, B. S.; Vullev, V. I.; Anvari, B. Revisiting Indocyanine Green: Effects of serum and physiological temperature on absorption and fluorescence characteristics. *IEEE J. Sel. Top. Quant.* 2014, 20.
56. Kasha, M.; Rawls, H. R.; Ashraf El-Bayoumi, M. The exciton model in molecular spectroscopy. *Eighth EUCMOS* 1965, 371-392.
57. Herzog, M.; Gerard, D.; Hirth, L.; Laustriat, G. Natural fluorescence properties of Brome Mosaic-Virus protein. *Biochim. Biophys. Acta* 1977, 493, 167-177.
58. Zuckerfranklin, D. Endocytosis by human-platelets: Metabolic and freeze-fracture studies. *J. Cell Biol.* 1981, 91, 706-715.

59. Punnonen, E. L.; Ryhanen, K.; Marjomaki, V. S. At reduced temperature, endocytic membrane traffic is blocked in multivesicular carrier endosomes in rat cardiac myocytes. *Eur. J. Cell Biol.* 1998, 75, 344-352.
60. van Dam, G. M.; Themelis, G.; Crane, L. M. A.; Harlaar, N. J.; Pleijhuis, R. G.; Kelder, W.; Sarantopoulos, A.; de Jong, J. S.; Arts, H. J. G.; van der Zee, A. G. J.; Bart, J.; Low, P. S.; Ntziachristos, V. Intraoperative tumor-specific fluorescence imaging in ovarian cancer by folate receptor-alpha targeting: first in-human results. *Nat. Med.* 2011, 17, 1315-1319.
61. Kosaka, N.; Mitsunaga, M.; Longmire, M. R.; Choyke, P. L.; Kobayashi, H. Near infrared fluorescence-guided real-time endoscopic detection of peritoneal ovarian cancer nodules using intravenously injected indocyanine green. *Int. J. Cancer* 2011, 129, 1671-1677.
62. Matsumura, Y.; Maeda, H. A new concept for macromolecular therapeutics in cancer-chemotherapy- Mechanism of tumorotropic accumulation of proteins and the antitumor agent smancs. *Cancer Res.* 1986, 46, 6387-6392.
63. Aina, O. H.; Marik, J.; Gandour-Edwards, R.; Lam, K. S. Near-infrared optical imaging of ovarian cancer xenografts with novel alpha 3-integrin binding peptide "OA02". *Mol. Imaging* 2005, 4, 439-47.
64. van Scheltinga, A.; van Dam, G. M.; Nagengast, W. B.; Ntziachristos, V.; Hollema, H.; Herek, J. L.; Schroder, C. P.; Kosterink, J. G. W.; Lub-de Hoog, M. N.; de Vries, E. G. E. Intraoperative near-infrared fluorescence tumor imaging with vascular endothelial growth factor and human epidermal Growth Factor Receptor 2 targeting antibodies. *J. Nucl. Med.* 2011, 52, 1778-1785.
65. Corbin, I. R.; Ng, K. K.; Ding, L. L.; Jurisicova, A.; Zheng, G. Near-infrared fluorescent imaging of metastatic ovarian cancer using folate receptor-targeted high-density lipoprotein nanocarriers. *Nanomedicine* 2013, 8, 875-890.
66. Yu, J.; Javier, D.; Yaseen, M. A.; Nitin, N.; Richards-Kortum, R.; Anvari, B.; Wong, M. S. Self-assembly synthesis, tumor cell targeting, and photothermal capabilities of antibody-coated Indocyanine Green nanocapsules. *J. Am. Chem. Soc.* 2010, 132, 1929-1938.
67. Chen, W. X.; Bardhan, R.; Bartels, M.; Perez-Torres, C.; Pautler, R. G.; Halas, N. J.; Joshi, A. A molecularly targeted theranostic probe for ovarian cancer. *Mol. Cancer Ther.* 2010, 9, 1028-1038.
68. Gupta, S.; Chatni, M. R.; Rao, A. L. N.; Vullev, V. I.; Wang, L. H. V.; Anvari, B. Virus-mimicking nano-constructs as a contrast agent for near infrared photoacoustic imaging. *Nanoscale* 2013, 5, 1772-1776.

69. Ma, Y. J.; Nolte, R. J. M.; Cornelissen, J. Virus-based nanocarriers for drug delivery. *Adv. Drug Del. Rev.* 2012, 64, 811-825.
70. Young, M.; Willits, D.; Uchida, M.; Douglas, T. Plant viruses as biotemplates for materials and their use in nanotechnology. *Annu. Rev. Phytopathol.* 2008, 46, 361-384.
71. Gill, S. C.; Vonhippel, P. H. Calculation of Protein Extinction Coefficients from Amino-Acid Sequence Data. *Anal. Biochem.* 1989, 182, 319-326.
72. Pace, C. N.; Vajdos, F.; Fee, L.; Grimsley, G.; Gray, T. How to Measure and Predict the Molar Absorption-Coefficient of a Protein. *Protein Sci.* 1995, 4, 2411-2423.
73. Schneider M., P. S., UniProt Consortium. UniProtKB amid the turmoil of plant proteomics research front. *Front. Plant Sci.* 3, 270-270.
74. Lucas, R. W.; Kuznetsov, Y. G.; Larson, S. B.; McPherson, A. Crystallization of brome mosaic virus and T=1 brome mosaic virus particles following a structural transition. *Virology* 2001, 286.
75. Larson, S. B.; Lucas, R. W.; McPherson, A. Crystallographic structure of the T=1 particle of brome mosaic virus. *J. Mol. Biol.* 2005, 346.
76. Li, M.; Guha, S.; Zangmeister, R.; Tarlov, M. J.; Zachariah, M. R. Method for Determining the Absolute Number Concentration of Nanoparticles from Electrospray Sources. *Langmuir* 2011, 27, 14732-14739.
77. Weissleder, R. A clearer vision for in vivo imaging. *Nat Biotech* 2001, 19, 316-317.
78. Saxena, V.; Sadoqi, M.; Shao, J. Indocyanine green-loaded biodegradable nanoparticles: preparation, physicochemical characterization and in vitro release. *Int. J. Pharm.* 2004, 278, 293-301.
79. Rodriguez, V. B.; Henry, S. M.; Hoffman, A. S.; Stayton, P. S.; Li, X.; Pun, S. H. Encapsulation and stabilization of indocyanine green within poly(styrene-alt-maleic anhydride) block-poly(styrene) micelles for near-infrared imaging. *Journal of Biomedical Optics* 2008, 13, 014025-014025-10.
80. Kim, T.; Chen, Y.; Mount, C.; Gombotz, W.; Li, X.; Pun, S. Evaluation of Temperature-Sensitive, Indocyanine Green-Encapsulating Micelles for Noninvasive Near-Infrared Tumor Imaging. *Pharm. Res.* 2010, 27, 1900-1913.
81. Wu, L.; Fang, S.; Shi, S.; Deng, J.; Liu, B.; Cai, L. Hybrid Polypeptide Micelles Loading Indocyanine Green for Tumor Imaging and Photothermal Effect Study. *Biomacromolecules* 2013, 14, 3027-3033.

82. Derycke, A. S. L.; Kamuhabwa, A.; Gijssens, A.; Roskams, T.; De Vos, D.; Kasran, A.; Huwyler, J.; Missiaen, L.; de Witte, P. A. M. Transferrin-Conjugated Liposome Targeting of Photosensitizer ALPcS4 to Rat Bladder Carcinoma Cells. *J. Natl. Cancer Inst.* 2004, 96, 1620-1630.
83. Steinmetz, N. F. Viral nanoparticles as platforms for next-generation therapeutics and imaging devices. *Nanomedicine-Nanotechnology Biology and Medicine* 2010, 6.
84. Cho, C. F.; Sourabh, S.; Simpson, E. J.; Steinmetz, N. F.; Luyt, L. G.; Lewis, J. D. Molecular Targeted Viral Nanoparticles as Tools for Imaging Cancer. *Methods in molecular biology (Clifton, N.J.)* 2014, 1108, 211-230.
85. Steinmetz, N. F. Viral Nanoparticles in Drug Delivery and Imaging. *Mol. Pharm.* 2013, 10, 1-2.
86. Wen, A. M.; Lee, K. L.; Yildiz, I.; Bruckman, M. A.; Shukla, S.; Steinmetz, N. F. Viral Nanoparticles for In vivo Tumor Imaging. 2012, e4352.
87. Lewis, J. D.; Destito, G.; Zijlstra, A.; Gonzalez, M. J.; Quigley, J. P.; Manchester, M.; Stuhlmann, H. Viral nanoparticles as tools for intravital vascular imaging. *Nat. Med.* 2006, 12.
88. Pokorski, J. K.; Steinmetz, N. F. The Art of Engineering Viral Nanoparticles. *Mol. Pharm.* 2011, 8, 29-43.
89. Yildiz, I.; Tsvetkova, I.; Wen, A. M.; Shukla, S.; Masarapu, M. H.; Dragnea, B.; Steinmetz, N. F. Engineering of Brome mosaic virus for biomedical applications. *RSC Advances* 2012, 2, 3670-3677.
90. Tolmachev, V.; Wallberg, H.; Sandstrom, M.; Hansson, M.; Wennborg, A.; Orlova, A. Optimal specific radioactivity of anti-HER2 Affibody molecules enables discrimination between xenografts with high and low HER2 expression levels. *Eur. J. Nucl. Med. Mol. Imaging* 2011, 38.
91. Booksh, K. S.; Muroski, A. R.; Myrick, M. L. Single-Measurement Excitation/Emission Matrix Spectrofluorometer for Determination of Hydrocarbons in Ocean Water. 2. Calibration and Quantitation of Naphthalene and Styrene. *Anal. Chem.* 1996, 68, 3539-3544.
92. Landsman, M. L. J.; Kwant, G.; Mook, G. A.; Zijlstra, W. G. LIGHT-ABSORBING PROPERTIES, STABILITY, AND SPECTRAL STABILIZATION OF INDOCYANINE GREEN. *J. Appl. Physiol.* 1976, 40, 575-583.
93. Yuan, B.; Chen, N.; Zhu, Q. Emission and absorption properties of indocyanine green in Intralipid solution. *Journal of biomedical optics* 2004, 9, 497-503.

94. Bae, P.; Jung, J.; Chung, B. Highly enhanced optical properties of indocyanine green/perfluorocarbon nanoemulsions for efficient lymph node mapping using near-infrared and magnetic resonance imaging. *Nano Convergence* 2014, 1, 1-10.
95. Kosaka, N.; Mitsunaga, M.; Longmire, M. R.; Choyke, P. L.; Kobayashi, H. Near infrared fluorescence-guided real-time endoscopic detection of peritoneal ovarian cancer nodules using intravenously injected indocyanine green. *Int. J. Cancer* 2011, 129, 1671-1677.